uc3m | Universidad Carlos III de Madrid

Bachelor's Degree in Aerospace Engineering
2016/2017

Bachelor Thesis

Characterization of electric propulsion plasma jet by means of Optical Emission Spectroscopy

---

Ana Isabel Torres Guijarro

Supervisor: Yacine Babou
Leganés (Madrid)
July 2017

Universidad Carlos III de Madrid

Abstract

Escuela Politécnica Superior

Bioengineering and Aerospace Engineering Department: Bacherlor's Degree in Aerospace Engineering

Ana Isabel Torres Guijarro

The aim of this project is to create a computational tool in MATLAB to build the image of a plasma jet by means of Optical Emission Spectroscopy with the objective to contribute to the plasma space propulsion systems development. This tool uses data from computer plasma jet simulations performed in EP2PLUS and spectral data from NIST Atomic Spectral Database together with a few parameters set by the user to build the desired plasma image in real colors. To do so, under the assumption of Local Thermodynamic Equilibrium, the tool uses Boltzmann distribution and the Emission equation to calculate the local densities and emissions in the jet, respectively. Once obtained, the intensities with the desired projection angle are computed by means of the Radon transform. They are then filtered by the human eye intensity curves to discard those emissions which cannot be detected by the human eye. The fraction of each color (Red, Green and Blue) on each projected surface unit is calculated and scaled to avoid image saturation. The resulting temperatures, spectra and images are shown and discussed in this thesis.

Universidad Carlos III de Madrid

Resumen

Escuela Politécnica Superior

Departamento de Bioingeniería e Ingeniería Aeroespacial: Grado en Ingeniería Aeroespacial

Ana Isabel Torres Guijarro

El objetivo de este proyecto es la creación de una herramienta de cálculo en MATLAB que represente la imagen de un chorro de plasma usando Espectroscopía Óptica con el fin de contribuir al desarrollo de los sistemas de propulsión por plasma. Esta herramienta usa datos obtenidos a partir de simulaciones por ordenador llevadas a cabo en EP2PLUS y datos espectrales de la base de datos NIST Atomic Spectral Database junto con algunos parámetros definidos por el usuario de la herramienta para obtener la imagen deseada en colores reales. Para ello, asumiendo condiciones de equilibrio termodinámico local (LTE), la herramienta usa la distribución de Boltzmann y la ecuación de la emisión para calcular las densidades y emisiones locales del chorro. Una vez obtenidas, se calculan las intensidades proyectadas con el ángulo deseado usando la Transformada de Radon. Después, éstas se filtran usando las curvas de intensidad del ojo humano para descartar las emisiones que no podrían ser detectadas por el ojo. Finalmente, se calcula la fracción de cada color (rojo, verde y azul) por unidad de superficie y se escala para evitar la saturación de la imagen para acabar mostrando las temperaturas, espectros e imágenes obtenias en el presente informe de este Trabajo de Fin de Grado.

Contents

List of Figures

List of Tables

Chapter 1

Introduction

The aim of this project is the creation of a computational tool to build the image of a plasma jet and analyze its spectra using Optical Emission Spectroscopy. The tool has been created in MATLAB environment and it is completely prepared for the user to enter the region of interest both in the spectral and in the spacial domain.

The present report is divided into 9 chapters whose main objectives are summarized below:

- In the present chapter, plasma is introduced, as well as those diagnostic methods and applications related with the scope of this project. Moreover, this chapter includes a brief summary of the general inputs and outputs that the tool provides, which helps the user understand the point of the tool from a very high perspective.

- In the second chapter, the background used to obtain the final results is explained. This includes the physical principles and laws together with the basic concepts that need to be understood before starting the tool generation.

- The third chapter is devoted to the implementation of principles and laws such as Boltzmann distribution or the line broadening mechanism considered in this project. Also, the MATLAB functions used to build the emission distributions are introduced and explained.

- The fourth chapter is devoted to explain how the intensity profiles have been built. The MATLAB commands used to obtain the intensity distribution are explained in detail together with the filter and the filtering procedure used to select the intensity seen in the resulting images.

- This fifth section covers the assessment of the code which includes the final results of this project. After introducing the set of data which are the input of the code in this project, the spectra, the temperature and the images obtained as output are shown, discussed and analyzed from a physical point of view.

- The next section covers all the socioeconomic environment and impact including the budget devoted to the tool creation and the environmental, economical and social impacts that the development of plasma thrusters may have.

- The regulatory framework chapter includes the applicable standards and patents related to plasma thrusters.

- The future work chapter covers all the further work that can be done to improve the tool generated for this project.

- The conclusion chapter summarizes the project and remarks the goals achieved during the tool development.

1.1 Plasma

Plasma is a state of matter itself, different from solid, liquid or gaseous states, it is an electric conductive mixture which contains a great number of ions and electrons, hence, the fluid is said to be ionized. The concentration of both coexisting species is such that the net charge of the fluid is close to zero. Thus, the fluid is said to be quasi-neutral. However, since the particles are electrically charged, the collection of particles as a whole responds to the electromagnetic fields, grouping in electron clouds or ion beams when influenced by the former field.

For this reason, besides colliding, plasma particles have the ability to interact between one another under the influence of an electromagnetic field with the difficulty that these particles need to be treated in groups. Also, because of its low density and hot temperature in comparison to water or the air in the atmosphere, plasma is not considered a continuous fluid. These two features make plasma physics a very difficult field of study.

The term plasma was first used in 1927 by the Nobel Prize holder Irving Langmuir to name ionized gases. When the American scientist observed an analogy between the collective response of ionized gases present in electric discharges to external perturbations and the behavior of blood plasma, he adopted this term to refer to this kind of systems. Nowadays plasma physics is the result of years of research in several tracks such as nuclear energy or electric propulsion.

1.1.1 Plasma applications

Far from being just present in nature, plasma has been used by human beings to develop widely used devices such as fluorescent lights or electric arc welders. However, the most promising plasma applications are in the production of energy through nuclear fusion and in spacecraft propulsion, which is the target field of this thesis and which will be treated in more detail in the next subsection.

1.1.2 Propulsion systems: plasma engines vs. chemical engines

In order to start the discussion about chemical and plasma propulsive systems, it is necessary to make a distinction between space rockets and rocket launchers. Rocket launchers are those responsible for orbiting the spacecraft from the surface of the Earth. Therefore, this kind of rockets need a huge propulsive force during a short period of time in order to overcome gravity and exit the Earth's atmosphere. Chemical engines are the only ones able to provide such a great thrust. In contrast, space rockets are used to move and control the position while in space.

Hence, plasma engines are just being developed for space rocket purposes.

Figure 1.1: Alliance Atlas 5 rocket launch from Cape Canaveral, FL [16]

Rocket engines are characterized by carrying the propellant stored in rocket tanks at the time of launch. A significant fraction of the propellant carried in the tanks is used to move the spacecraft while in space. Thus, one of the most important costs and challenges for a space mission is to launch the rocket. The heavier it is, the greater the force is needed to overcome gravity during the launch.

In chemical rockets, the specific impulses are set by the propellant, which has an impulse ceiling related to its heating value. Therefore, it is not possible to achieve higher specific impulses by modifying parameters during the combustion. Nevertheless, in plasma rockets, the specific impulse is not related to the propellant but to the electromagnetic discharges provided. Hence, plasma rockets are able to generate huge specific impulses that have been already tested in the space environment.

This, together with the advantage of decreasing the propellant mass during the entire mission, reducing consequently the mission expenses, make plasma propulsion an interesting field of study. However, there is a limitation in the power available to start the electromagnetic discharges. The power can be measured as a first approach as follows:

$$P \propto I \cdot F \tag{1.1}$$

Being I the specific impulse and F the thrust. Since the specific impulse (I) given by the plasma thrusters is considerably high, the thrust is reduced in comparison to a chemical thruster. Therefore, the time it takes for the spacecraft to complete its mission increases.

In a plasma thruster, the propellant is bombarded with electrons until it is ionized due to the collisions between particles. The electrons are kept the longest possible in the discharge chamber by using strong magnetic fields, increasing this way the probability of colliding with unionized propellant.

Once the positive ions are obtained, they are accelerated to the exhaust of the engine as an ion rod, therefore producing thrust. In the same way and in order to maintain the quasi-neutral state of the thruster, the neutralizer is in charge of accelerating the same amount of electrons out of the engine.

As an example of this kind of thruster, NASA is developing the Variable Specific Impulse Plasma Thruster (VASIMR) for Martian missions. The parts of this electromagnetic plasma thruster are shown in Figure 1.2.

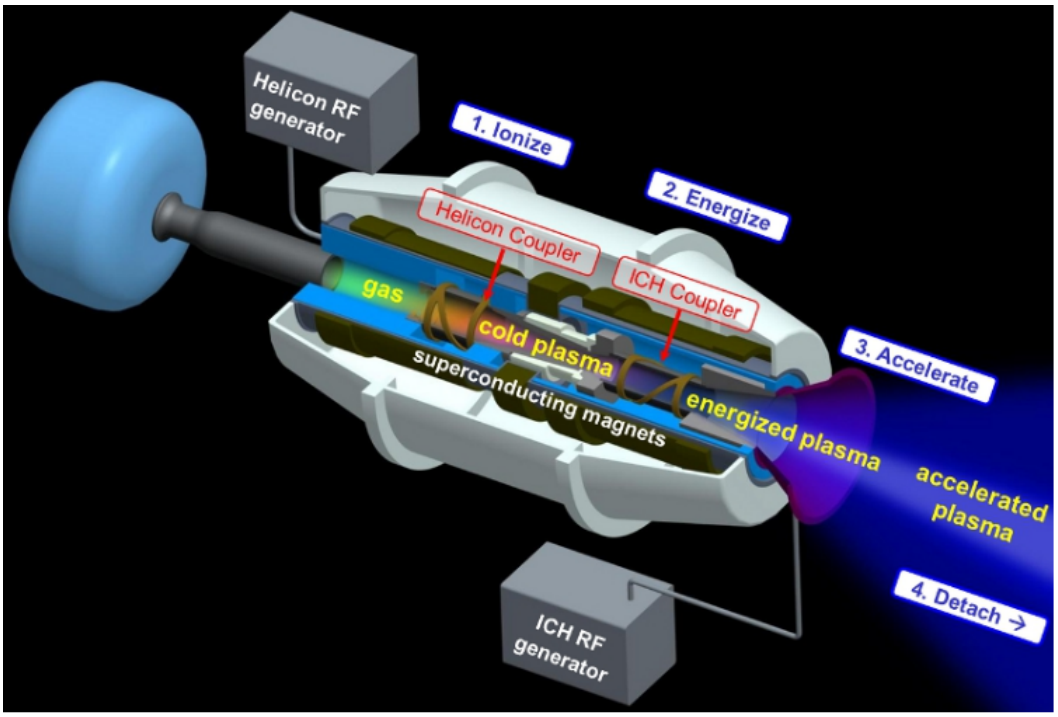

Figure 1.2: VASIMR electromagnetic plasma engine [17]

1.1.3 Plasma diagnostics

Plasma diagnostic methods are a set of techniques used to obtain various properties of the plasma that is being studied with the aim to better characterize the material. There are a great set of plasma diagnostic methods and the plasma properties obtained in the characterization depend upon the technique used in the diagnostics. However, this project is focused on the spectroscopic diagnostic techniques. Therefore, a more detailed explanation about this kind of techniques is introduced in this section.

Optical Emission techniques are considered to be useful for qualitative characterization of plasma. Since plasma reactions emit radiation with a frequency that ranges in the spectrum from the IR to the UV frequencies, there is a way of optical characterization by means of spectroscopy. This non-intrusive plasma diagnostics technique groups those plasma diagnostic methods based on the radiation emitted by the primary gas atoms when they lose electrons to ionize and finally become plasma.

There are some other important plasma diagnostics techniques such as the Langmuir Probe, which is an intrusive electric technique and some other non-intrusive optical methods such as the tomography.

1.2 The computational tool

As it has been previously explained, this thesis aims to build a computational tool to determine the local radiative properties of a generic plasma jet produced by an Electric Propulsion system in order to help qualify the radiative losses and intensity distributions.

The tool contributes to the development of plasma thrusters for spacecraft. Since this technology is very new, there is not much research about tools to obtain the image of a plasma jet in the aerospace community. Therefore, the state of the art of this kind of tools could be extrapolated to its context: plasma thrusters, whose degree of development has been explained in previous sections of this introduction chapter.

In order to help the user understand what needs to be provided to the code to obtain the desired results and as a first contact with the tool working conditions, figure 1.3 shows an schematic flow chart which explains the inputs needed and the outputs provided by the tool.

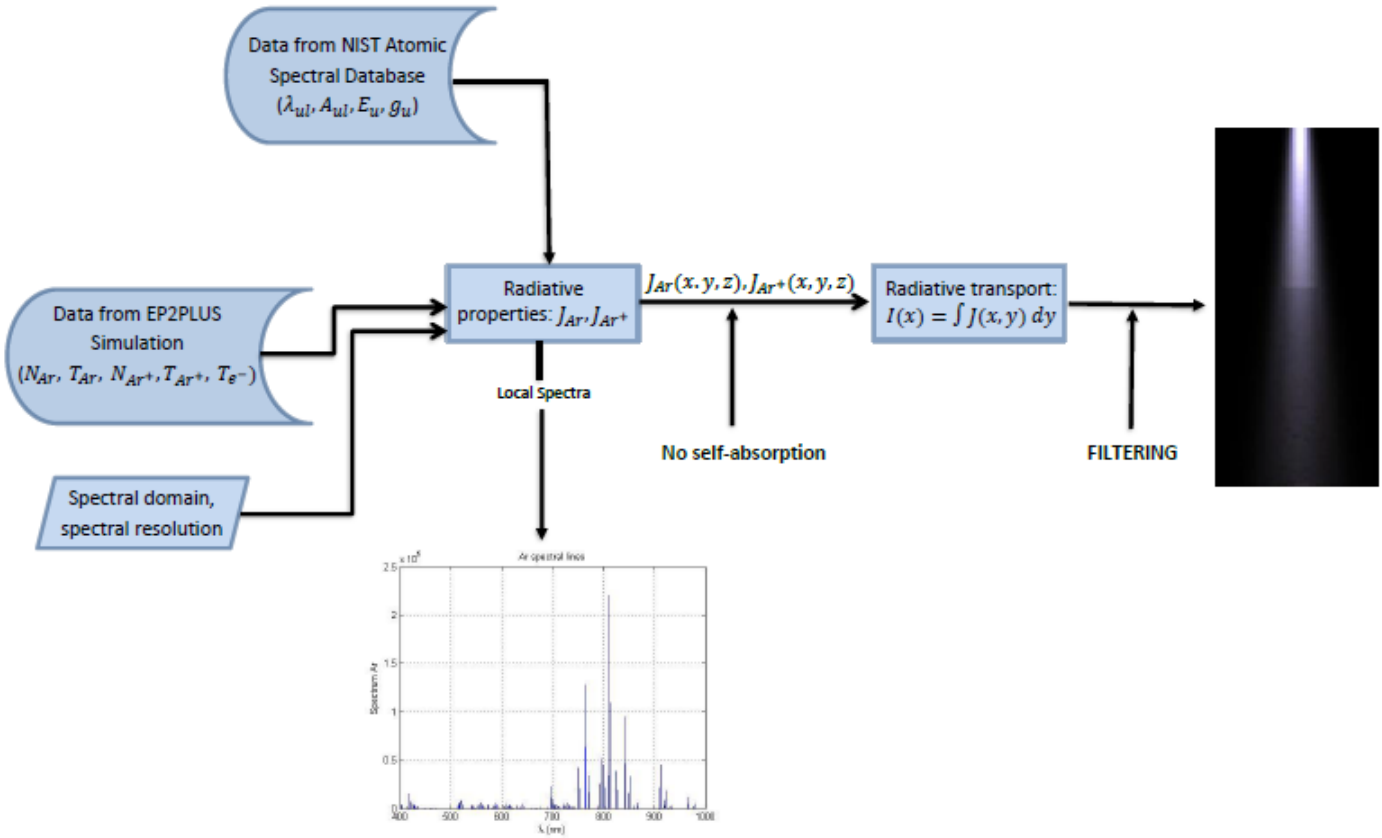

Figure 1.3: Flow chart of the computational tool

Chapter 2

Background

The aim of this chapter is to cover all the principles, concepts and equations that have been used for the development of the tool. The objective is to enlighten the reader with all the knowledge needed to understand the tool working principles.

2.1 Argon and its structure

Noble gases are the most stable particles in the periodic system. Since plasma is a state of matter that is still under investigation, the substances used for plasma thrusters are noble gases because their behavior is well-known. When ionized, noble gases will for sure attract the electron that they are missing, producing more and more collisions in the plasma, which will help the fluid be ionized for longer periods of time.

Nevertheless, there are six noble gases in the periodic system. Therefore, which one would be the best substance to be used as a propellant in a plasma thruster? There is one main factor that plays a significant role in this decision: its abundance in the Earth.

The selection of the substance used in the simulations is important for further laboratory experiments where this tool can be used. Therefore it is important to know its cost and abundance.

	Helium	Neon	Argon	Kripton	Xenon	Radon
Abundance (ppm)	5.20	18.20	9340,00	1,10	0,09	$(0.06 - 18)10^{-19}$
Price (USD/m^3)	4.20-4.90	22.30-44.90	2.70-8.50	60-120	400-500	4000-5000

Table 2.1: Abundance and Price of noble gases [24]

Table 2.1 shows the abundance of each noble gas in the Earth's atmosphere measured in parts per million (ppm) and the price per volume in 2004 of each noble gas. It can be clearly appreciated that Argon is the cheapest, most abundant noble gas in the Earth. Although this project can be carried out with any noble gas since this is a theoretical study, the aim of the computational tool is to be the base for experimental tests. Therefore, it is pretty easy to understand why Argon is the element chosen in this simulation.

Particles present internal energy levels known as quantum levels. This refers to the fact that the energy taken on by a particle is quantified. Among the energy levels, radiative processes take place which produce the spectral lines considered in this project. Thus, it is interesting to see the energy distribution in the atom of Argon. Figure 2.1 shows the diagram of Argon energy levels, where E is the energy in a specific quantum level.

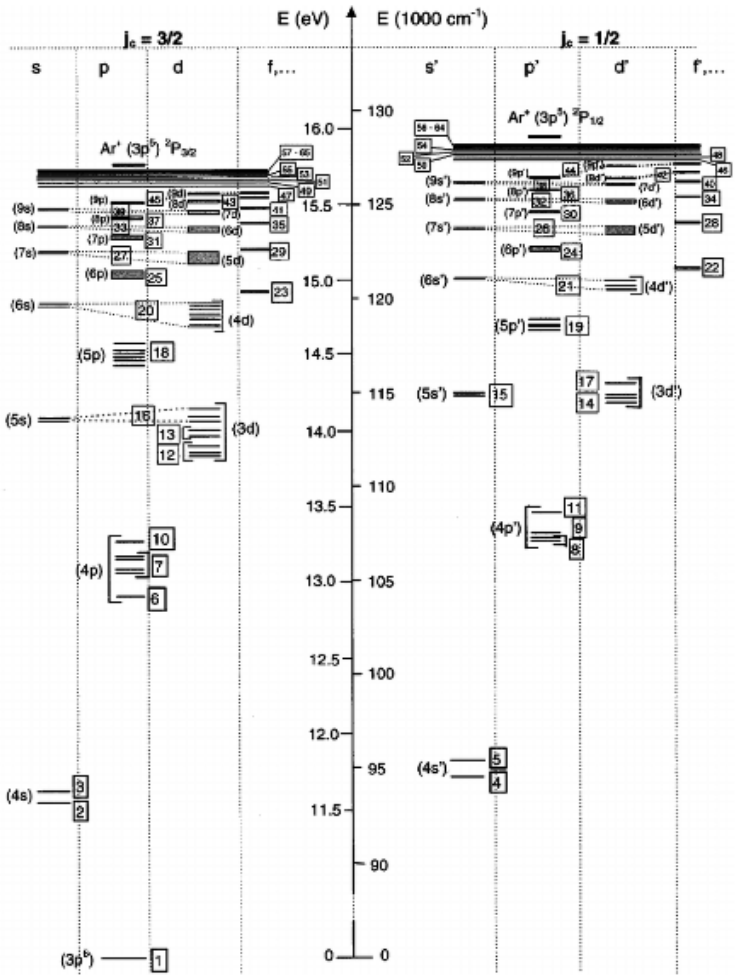

Figure 2.1: Argon energy levels [20]

The ionization energy (E_I) is defined as the energy required to remove the most loosely held electron from a gaseous atom. The reaction related to the removal of one electron is expressed below:

$$A + \Delta E_I \rightarrow A^+ + e^- \tag{2.1}$$

In the same way, if instead of losing one electron, the electron goes from a lower quantum level to an upper quantum level, a specific amount of energy is required and it has to be provided to the atom, in the case of plasma thrusters, via electric discharges. The amount of energy that is needed by the different noble gas species

can be inferred by establishing an analogy between the removal of electrons and the electron transition to upper energy levels. The ionization energy of several elements including the noble gases are shown in figure 2.2.

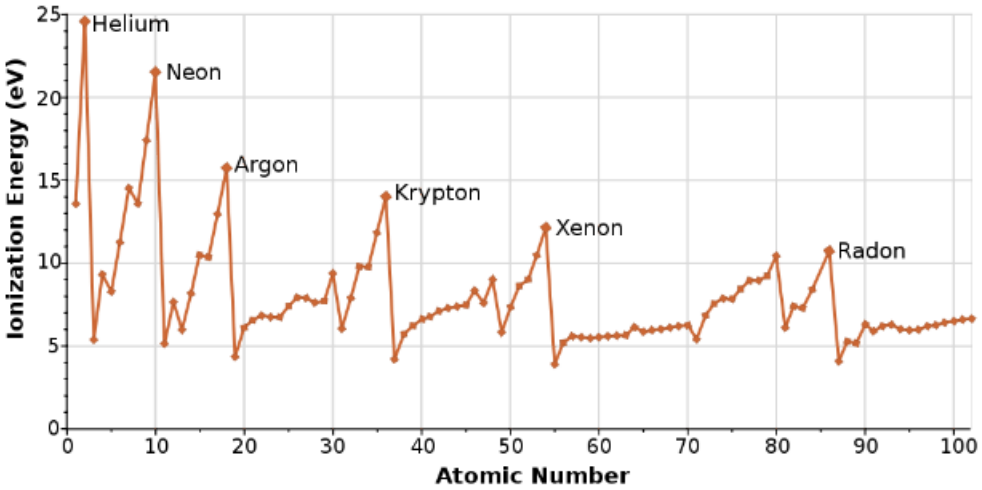

Figure 2.2: Ionization energies of noble gases and some important elements [21]

The energetic differences between them are due to the number of electrons that they have. As it can be seen, the decreasing ionization energy trend corresponds to the increase of electrons that atoms hold in their orbitals. Therefore, the electrostatic forces that the nucleus exerts on the electrons are lower due to the distance between the nucleus and the electrons in the further level, making the atom easier to ionize.

The atomic structure of Argon corresponds to a nucleus with 18 protons surrounded by 18 electrons as it can be seen in figure 2.3. The electrons in the outermost orbitals are the easiest to excite and separate from the core, creating an ion (Ar^+).

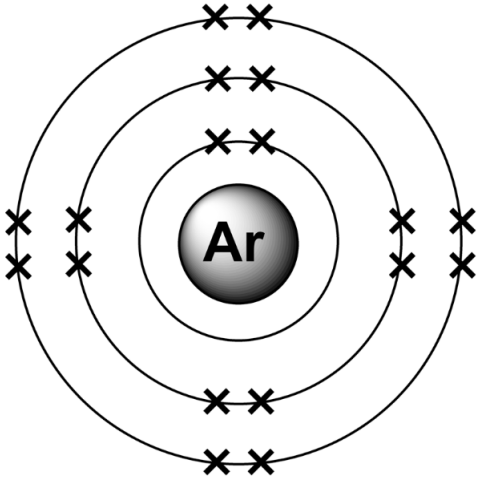

Figure 2.3: Electronic configuration of Argon [19]

2.2 Radiative Mechanisms

As mentioned in the previous section, in molecular and atomic scale, the energy is quantized. Electron transitions between atomic levels occur through absorption, spontaneous emission or induced emission. These radiative processes take place following Planck's law; when a photon is moving with a frequency such that the energy resulting from that movement is equal to the energy difference between two specific atomic levels:

$$E = h\nu \tag{2.2}$$

Equation 2.2 provides the energy (E) of a photon, which comes from the product of the Planck's constant (h), which is equal to $6.62607004 \times 10^{-34} \left[\frac{m^2 \cdot kg}{s}\right]$ and the frequency of oscillations of the photon (ν).

- **Absorption:** Absorption consists on the transition of an electron from a lower to an upper quantum level. Therefore, the energetic state of the atom increases. This occurs when the energy of the photon accurately matches the energy difference between the two atomic levels involved in the transition.

- **Spontaneous emission:** Emission refers to the transition of an electron from an upper to a lower quantum energy level. Atoms and molecules tend to be in the lowest possible energy state, well-known as ground state. Moreover, when an electron is in an excited state and it spontaneously decays to a lower energy state, a photon is released.

- **Induced or stimulated emission:** Recalling the definition of emission explained in the previous part. When an electron is in a high energy state, then a photon with a quantum energy equal to the energy gap between the quantum levels may induce the electron drop to a lower level, releasing two photons with the same quantum energy.

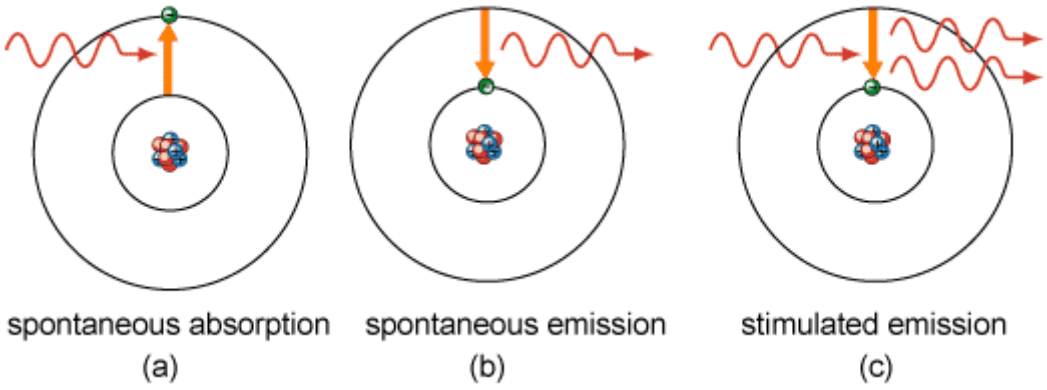

Figure 2.4: Schemes of the three radiative processes [23]

Through the three radiative processes previously described, this project is focused on the spontaneous emission, since it is the process responsible for the emitted light in the plasma under investigation.

When an electron passes from an upper level to a lower level it emits a photon of equal energy than the energy difference between the quantum levels. This can be expressed as:

$$E_u - E_l = h\nu_{ul} = E_{photon} \tag{2.3}$$

The radiative processes are described by the Einstein coefficients that refer to the probability per unit time that an electron in an excited state will spontaneously fall to a low-energy level, hence, emitting a photon. The Einstein coefficients that correspond to the spontaneous emission process are denoted by A_{ul} and measured in s^{-1}. Therefore, they are the ones used in this project, which have been obtained from the NIST Atomic Spectra Database as explained in chapter 5.

2.3 Spectroscopy

Spectroscopy studies the interaction between electromagnetic radiation and matter. It normally displays radiation intensity as a function of the wavelength. As it has already been mentioned, this project takes into account spectral lines originated in the spontaneous emission of photons. More specifically, Optical Emission Spectroscopy is used in the present project to analyze Argon plasma.

The emitted radiation can be analyzed by means of the spectral lines that it produces. When a photon is emitted, a spike will appear in the corresponding spectrum. This spike, corresponding to the emission, will have a specific frequency (ν_{ul}) that is determined by the Planck's law in equation 2.2. That frequency (ν_{ul}) is directly related to the length (λ_{ul}) of the electromagnetic wave as shown in equation 2.4.

$$\lambda_{ul} = \frac{c}{\nu_{ul}} \tag{2.4}$$

Were c is the speed of light equal to $3 \cdot 10^8$ [m/s].

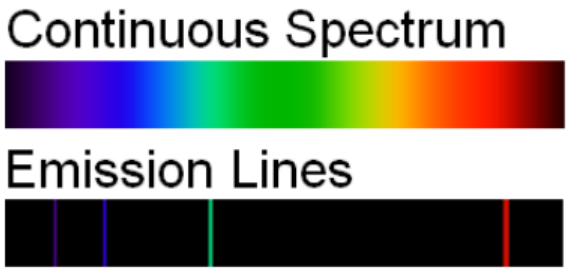

Figure 2.5: Emission lines compared to the continuous visible spectrum [25]

2.4 Boltzmann Distribution

A plasma is said to be in Thermodynamic Equilibrium (TE) if its collisional and radiative processes are balanced due to their reverse reactions. However, since this total equilibrium condition is hard to be achieved in laboratory tests, the Local Thermodynamic Equilibrium (LTE) is considered. In LTE, the collisional processes are balanced by means of plasma recombination while the radiative processes are not. Considering the unbalanced radiative processes, the plasma in Local Thermodynamic Equilibrium emits photons which make possible the spectroscopic analysis of the plasma jet.

In LTE, the same laws that can be used in total thermodynamic equilibrium govern, except for the one related to radiation. Therefore, under the assumption of LTE, Boltzmann Distribution equation is applied to this simulation in order to calculate the particle density distribution in a specific energy level (N_i).

$$N_i = \frac{N}{Q} g_i e^{\frac{-E_i}{k_B T_{ex}}} \tag{2.5}$$

Where:

- N is the total number of Ar or Ar^+ particles in each unit of volume defined in the jet measured in m^{-3}.

- Q is the partition function.
- g is the degeneracy.
- E_i is the internal energy in level i measured in cm^{-1}.
- k_B is the Boltzmann constant measured in $\frac{m^2 kg}{s^2 K}$.
- T_{ex} is the electron temperature distribution measured in K.

The corresponding factor has been applied in this expression in order to account for the unit changes. This will be specified in the next chapter.

2.5 Local Emission

In this project, the local emission distribution is calculated following equation 2.6, which shows the local emission for a given electronic transition from an upper quantum level (u) to a lower energy level (u). That is, for an electronic transition $u \rightarrow l$:

$$J_{ul} = \frac{1}{4\pi} N_u A_{ul} h \nu_{ul} \tag{2.6}$$

Where:

- N_u is the number of particles in level u per unit volume, which is measured in m^{-3}.
- A_{ul} is the Einstein coefficient for spontaneous emission from u to l, which is measured in s^{-1}.
- h is the Planck's constant measured in $\frac{m^2 kg}{s}$.
- ν_{ul} is the reference frequency for each spectral line measured in s^{-1}.

2.6 Types of Broadening in emission spectral lines

Ideally, the spectral lines are expected to be infinitely narrow and corresponding just to a single wavelength. In reality, the photon energies are spreaded around the ideal spectral line. This results in the so-called broadening, which are produced by non-zero values for the emission for wavelengths close to the reference one (λ_{ul}).

In practice, there are different types of broadening processes. These can be classified in:

- Microscopic processes: These are those broadening processes that take place in scales shorter than the photon mean free path.
- Macroscopic processes: These are those broadening processes that take place in scales larger than the photon mean free path.
- Instrumental processes: These processes are a kind of macroscopic processes that are considered as a separated group due to their artificial nature.

The present study is focused on the microscopic group of broadening processes in which several particular processes can be distinguished.

- First, the collisional broadening. When the observed atoms or ions are suffering continuous collisions with other particles, the energy levels are distorted causing a broadening in the emission lines with Lorentzian shape. Nevertheless, for the present project, this effect is neglected because it is only significant in a dense gas. Since the simulations assume a vacuum environment, this type of broadening can be considered negligible.

- Second, the natural broadening. As the Heisenberg uncertainty principle states: The energy of a level is uncertain by an amount of ΔE.

$$\Delta E \Delta t \approx \frac{h}{2\pi} \tag{2.7}$$

The energy level of an excited state of an atom or ion cannot be determined in a precise way because the atom is not infinitely excited. Therefore, the profile is spreaded over the ideal line at λ_{ul} in the shape of a Lorentzian.

Nonetheless, in this project, for the sake of simplicity and since the natural broadening is not the dominant effect in this plasma jet, this broadening mechanism is neglected.

- Third, the Doppler or thermal broadening. Doppler broadening occurs due to the motion of the atoms relative to the observer. The observed photons inside the atoms or molecules do not have the same frequency as the emitted photons due to the Doppler effect. In the present project, the thermal broadening is the dominant effect.

2.6.1 Doppler effect or Thermal Broadening

Despite being considered one of the simplest line broadening mechanisms, the Doppler effect is one of the most common and significant line broadening methods. As previously explained, when an atom is in thermal motion, the frequency of emission in its own reference system is different from the frequency perceived by the observer.

When this situation takes place, there is a frequency shift that is different for every atom. Thus, the spectral lines suffer a broadening that needs to be studied. The displacement that the frequency of each atom suffers can be expressed as follows:

$$\nu - \nu_{ul} = \frac{\nu_{ul} V}{c} \tag{2.8}$$

Where ν_{ul} corresponds to the reference frequency of the photon, ν is the frequency perceived by the observer and the one used to calculate the wavelengths for emission spikes, V is the velocity at which the atom is moving and c is the speed of light.

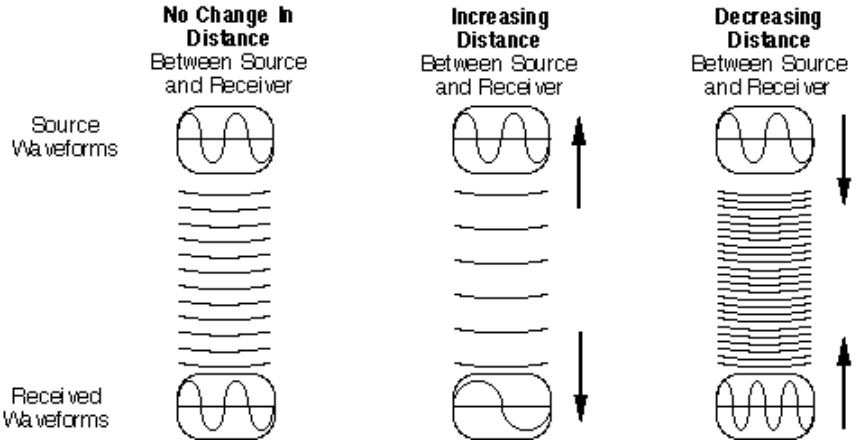

Figure 2.6: Doppler effect [27]

Moreover, the frequency shift follows a specific pattern that can be observed in figure 2.6: when the atom is moving towards the observer, the length of the electromagnetic wave that the observer receives increases, hence, decreasing the frequency. When the atom is moving away from the receiver, the perceived wavelength is reduced.

2.7 Energy conservation

The purpose of this section is to explain the energy conservation principle in which the spectral distributions are based. Given a x, y, z position, this principle states that for a specific spectral domain and a set of spectral lines, regardless the spectral resolution taken and the broadening mechanism, the energy is in every case

conserved. Hence, considering one single electron transition:

$$\int_{\lambda_{min}}^{\lambda_{max}} f(\lambda, x, y)d\lambda = \int_{\lambda_{min}}^{\lambda_{max}} A_{ul} \cdot h \cdot \frac{c}{\lambda_{ul}} \cdot N_u(x, y) \cdot f_D(\lambda - \lambda_{ul})d\lambda \tag{2.9}$$

Where $f(\lambda, x, y)$ is the resulting emission once the line broadening mechanism has been applied and $f_D(\lambda - \lambda_{ul})$ is the term that refers to the Doppler profile, which is in charge of distributing the energy through the spectral grid. Since this term has been normalized ($\int f_D(\lambda - \lambda_{ul})d\lambda = 1$), equation 2.9 can be expressed as 2.10:

$$\int_{\lambda_{min}}^{\lambda_{max}} f(\lambda, x, y)d\lambda = A_{ul} \cdot h \cdot \frac{c}{\lambda_{ul}} \cdot N_u(x, y) \tag{2.10}$$

This principle is the one that allows the use of the Doppler profile in this project since the thermal broadening does not change the energy in the system, the energy is just distributed along the spectral domain but it is conserved since the Doppler profile is by definition normalized.

2.8 Intensity

The monochromatic intensity of the radiation emitted by the plasma jet acquired along a defined optical path is the result of the line integral of the emission as shown in equation 2.12.

$$I_\lambda(x) = \int_{y_{min}}^{y_{max}} J_\lambda(x, y)dy \tag{2.11}$$

However, for those cases in which the plasma jet is not symmetric, the intensity shown is dependent on the angle of projection. Hence, the intensity of all the spectral lines at a specific angle is calculated using the Radon Transform. This transform takes the line integral of a 2D function over that line, which integrated for every height of the jet gives 2D results, obtaining the projected data that would be the input in a project based on tomography. The projected intensity also depends on the self-absorption of the plasma jet, for simplicity, this tool assumes no self-absorption in the jet.

Considering a two dimensional local emission distribution referred as $J_\lambda(x, y)$ and obtained by the use of equation 2.6, this project deconstructs the emission distribution into its orthogonal projection on a plane perpendicular to a line passing through the origin with an angle θ so as to calculate the intensity profile $I_{\theta,\lambda}(x')$ for a specific spectral line.

$$I_{\theta,\lambda}(x') = \int_{y'_{min}}^{y'_{max}} J_\lambda(x'cos\theta - y'sin\theta, x'sin\theta + y'cos\theta)dy' \tag{2.12}$$

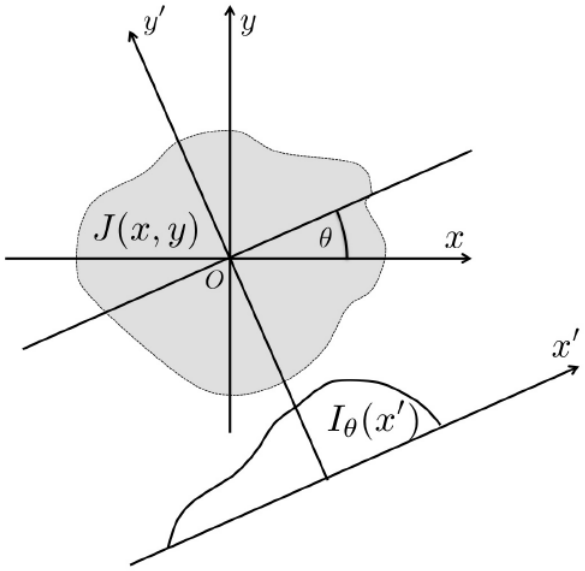

Figure 2.7: Intensity calculation principle

Where, as it can be appreciated from figure 2.7, θ corresponds to the angle between the $y - y'$ and $x - x'$ axis.

The use of Radon transform in this section makes possible to obtain the images from different angles, which is vital for the further analysis of the results.

Chapter 3

Local Emission Building

The aim of this section is to explain how the local emission spectra has been obtained in MATLAB based on the methods and principles detailed in the previous chapter.

First, the tool has a set of parameters that can be modified by the user for further experiments with a different or a similar flow field. Among this parameters, the spectral grid can be established by the user with the desired wavelength and resolution. In this particular project, the grid lower and upper limits have been set equal to 400 and 1000 nm, respectively. The reason why these limits have been chosen is that the reference wavelengths at which electronic transitions take place are concentrated in this spectral domain.

Despite the fact that the reference wavelengths, which have been obtained from the NIST Atomic Spectral Database present an accuracy of $\Delta grid = \pm 0.0001 nm$, for the sake of simplicity and in order to save computational time, the reference wavelengths have been crudely rounded to an accuracy of $\Delta grid = \pm 1 nm$.

Second, as a result of the previous action, the maximum spectral resolution that can be used not to skip any spectral line and lose information is $\Delta grid = 1 nm$. Nevertheless, the user can set lower values for the spectral resolution, which will provide smoother resulting spectral lines as shown in chapter 5.

Third, it is necessary to set the parameter that defines the number of nodes in the (x, y) domain. This parameter is called *iresize* and it directly determines the size of data obtained from the simulation that are going to be considered for the calculations. Therefore, the total number of nodes in the (x, y) domain will be $N = iresize \times iresize$. In the case of choosing a different value for *iresize* than the size coming from the simulations, the MATLAB function `imresize` makes an approximation. This function returns a matrix that has the number of rows and columns required by the user, for this specific tool, *iresize* rows and columns.

Once these parameters have been set, the tool is able to calculate the number of particles in a specific energy level ($N_{u,Ar}(x, y), N_{u,Ar^+}(x, y)$) in each unit volume [V(x, y, z)] by means of equation 2.5, which is used for both Ar and Ar^+.

$$N_{u,Ar}(x,y) = \frac{N(Ar)}{Q} g_u(Ar) e^{\frac{-1.44E_u(Ar)}{k_B T_{e^-}(x,y)}} \tag{3.1}$$

$$N_{u,Ar^+}(x,y) = \frac{N(Ar^+)}{Q} g_u(Ar^+) e^{\frac{-1.44E_u(Ar^+)}{k_B T_{e^-}(x,y)}} \tag{3.2}$$

Where g_u is the degeneracy, E_u is the energy of the upper level, N is the total number of particles per unit volume, Q is the partition function and T_{e^-} is the local electron temperature. The factor that multiplies E_u accounts for the change of units in order to enter E_u in cm^{-1}.

For simplicity, in this project the partition function (Q) has been assumed to be constant and equal to 1 for Ar and 5 for Ar^+. These numbers have been estimated using a temperature of approximately 1eV. In practice, the partition function slightly varies with the temperature distribution.

Although expressions 3.1 and 3.2 calculate the Ar and Ar^+ density distribu-

tions in the (x, y) domain, the distribution for the entire volume is calculated by looping these expressions in MATLAB.

The next step is to calculate the local emission for a transition at a specific wavelength (λ_{ul}) following equation 2.6, which can be applied for ions and neutrals as follows:

$$J_{ul,Ar}(x,y) = \frac{1}{4\pi} N_{u,Ar}(x,y) A_{ul} h\nu_{ul} \tag{3.3}$$

$$J_{ul,Ar^+}(x,y) = \frac{1}{4\pi} N_{uAr^+}(x,y) A_{ul} h\nu_{ul} \tag{3.4}$$

Where the subindex "ul" refers to the upper $\rightarrow$ lower level transition: ν_{ul} is the reference frequency of each spectral line, which has been calculated with equation 2.4, A_{ul} is the Einstein coefficient of the transition and N_u is the density of the corresponding element in the upper level.

3.1 Spectra simulation: Doppler broadening

The emitted lines reach a peak at the reference wavelength (λ_{ul}). However, as explained in the previous chapter, the spectral lines are not completely narrow, the plasma effects are responsible for a broadening that in this case has been represented by means of a Doppler profile, neglecting the collisional broadening due to the low pressure levels in space and the natural broadening since it is not dominant. Through the thermal broadening or Doppler effect, the value for the emission line width is a key parameter for the evaluation of the spectral lines in the spectral grid defined by the user. This value is calculated as the Full Width at the Half Maximum (FWHM) of the spectral profile as follows:

$$FWHM_{Ar}(x,y) = \frac{7.15 \times 10^{-8}}{2\sqrt{2ln(2)}} \sqrt{\frac{T_{Ar}(x,y)}{m_{Ar}}} \lambda_{ul} \tag{3.5}$$

$$FWHM_{Ar^+}(x,y) = \frac{7.15 \times 10^{-8}}{2\sqrt{2ln(2)}} \sqrt{\frac{T_{Ar^+}(x,y)}{m_{Ar^+}}} \lambda_{ul} \tag{3.6}$$

Where T_{Ar} and T_{Ar^+} are refer to the local temperature of Ar and Ar^+, respectively, m_{Ar} and m_{Ar^+} are the mass of Ar and Ar^+, which have been set equal to 40 atomic mass units. Therefore, the factor that multiplies expressions 3.5 and 3.6 accounts for the the changes in units.

For each spectral line, a starting and ending value for the wavelength range has been established in advance as a function of the FWHM. In order to calculate the starting and ending values for each spectral line, another parameter has to be set by the user: $P_{broadening}$.

$$\lambda_{lower} = \lambda_0 - P_{broadening} \cdot FWHM \tag{3.7}$$

$$\lambda_{upper} = \lambda_0 + P_{broadening} \cdot FWHM \tag{3.8}$$

As seen in equations 3.7 and 3.8, this parameter selects the piece of spectral grid that the spectral Gaussian is going to cover when calculated. The user can set the parameter to any value although high values are recommended. In this project $P_{broadening} = 100$.

Finally, the code has sufficient information to generate the spectral lines for Ar and Ar^+ accounting for the Doppler profile by using the following expressions:

$$f_{Ar}(\lambda-\lambda_{ul})(x,y) = \frac{1}{FWHM_{Ar}(x,y)\sqrt{2\pi}} \times exp\left[-\frac{1}{2}\left(\frac{\lambda-\lambda_{ul}}{FWHM_{Ar}(x,y)}\right)^2\right] \quad (3.9)$$

$$f_{Ar^+}(\lambda-\lambda_{ul})(x,y) = \frac{1}{FWHM_{Ar^+}(x,y)\sqrt{2\pi}} \times exp\left[-\frac{1}{2}\left(\frac{\lambda-\lambda_{ul}}{FWHM_{Ar^+}(x,y)}\right)^2\right] \quad (3.10)$$

After the implementation of the Doppler broadening, the result of each spectral line is a sharp Gaussian. However, at this point, these Gaussians do not follow an homogeneous distribution in the spectral domain. Instead, they are a set of vectors that match some pieces of the spectral grid. Therefore, it is necessary to put together all the spectral lines for both Ar and Ar^+. With this purpose, the vectors $f_{ArSpectral}$ and $f_{Ar^+Spectral}$ have been created. These vectors have exactly the same number of elements as the spectral grid and they are set to zero to help create an homogeneous emission spectrum in a single vector.

$$f_{Ar}(\lambda,x,y) = f_{Ar}(\lambda-\lambda_{ul},x,y) + f_{ArSpectra}(\lambda,x,y) \quad (3.11)$$

$$f_{Ar^+}(\lambda,x,y) = f_{Ar^+}(\lambda-\lambda_{ul},x,y) + f_{Ar^+Spectra}(\lambda,x,y) \quad (3.12)$$

The result of equations 3.11 and 3.12 is a vector where the calculated broadened emission has been stored at the corresponding wavelength positions in the spectral grid and those wavelengths without an associated emission correspond to $f_{Ar}(\lambda,x,y) = 0$ or $f_{Ar^+}(\lambda,x,y) = 0$.

Now, in order to obtain a vector with all the spectral lines, the spectra of Ar

and Ar^+ are put together as follows:

$$f_{Ar\&Ar^+}(\lambda, x, y) = f_{Ar}(\lambda, x, y) + f_{Ar^+}(\lambda, x, y) \tag{3.13}$$

The result is a vector where the spectral lines of both Ar and Ar^+ are stored in the spectral range selected by the user.

3.2 Plasma characterization: Excitation temperature

The method used by this tool to obtain the excitation temperature of the plasma jet is Optical Emission Spectroscopy. From the spectral emission lines calculated by the tool in the spectral mode, the excitation temperature can be derived.

To do so, it is only necessary to consider two electron transitions which have sufficient differences in the energy of the upper level. Equations 3.14 and 3.15 refer to the complete emission equation for emission lines n and n+1 respectively.

$$J_{ul}^{n} = \frac{N}{Q} \cdot g_u^n \cdot exp\left[\frac{-E_u^n}{T_{ex}}\right] \cdot h \cdot \nu_{ul}^n \cdot A_{ul}^n \tag{3.14}$$

$$J_{ul}^{n+1} = \frac{N}{Q} \cdot g_u^{n+1} \cdot exp\left[\frac{-E_u^{n+1}}{T_{ex}}\right] \cdot h \cdot \nu_{ul}^{n+1} \cdot A_{ul}^{n+1} \tag{3.15}$$

The spacial point at which the electron temperature is calculated is the same

for both electron transitions. Therefore, it is possible to obtain the electron temperature by combining the equations above as follows:

$$\frac{J_{ul}^{n+1}}{J_{ul}^{n}} = \frac{g_u^{n+1}}{g_u^n} \cdot exp\left[\frac{E_u^n - E_u^{n+1}}{T_{ex}}\right] \cdot \frac{\nu_{ul}^{n+1}}{\nu_{ul}^n} \cdot \frac{A_{ul}^{n+1}}{A_{ul}^n} \tag{3.16}$$

$$\frac{[E_u^n - E_u^{n+1}]}{T_{ex}} = log\left(\frac{J_{ul}^{n+1}}{J_{ul}^n} \cdot \frac{g_u^n}{g_u^{n+1}} \cdot \frac{\nu_{ul}^n}{\nu_{ul}^{n+1}} \cdot \frac{A_{ul}^n}{A_{ul}^{n+1}}\right) \tag{3.17}$$

$$T_{ex} = \frac{[E_u^n - E_u^{n+1}]}{log\left(\frac{J_{ul}^{n+1}}{J_{ul}^n} \cdot \frac{g_u^n}{g_u^{n+1}} \cdot \frac{\nu_{ul}^n}{\nu_{ul}^{n+1}} \cdot \frac{A_{ul}^n}{A_{ul}^{n+1}}\right)} \tag{3.18}$$

The excitation temperature is obtained as the inverse of the slope of the so-called Boltzmann plot, which relates $log\left(\frac{J_{ul}^{n+1}}{J_{ul}^n} \cdot \frac{g_u^n}{g_u^{n+1}} \cdot \frac{\nu_{ul}^n}{\nu_{ul}^{n+1}} \cdot \frac{A_{ul}^n}{A_{ul}^{n+1}}\right)$ with $E_u^n - E_u^{n+1}$. At least two electron transitions need to be considered for the derivation of the excitation temperature, although the greater the number of transitions, the more accurate the value for the Boltzmann plot slope and excitation temperature.

This method is interesting because it is able to obtain relevant information when local emission is known. This is a valid approach when the intensity gradients are weak enough to consider that the intensity is merely proportional to the local emission. However, it the gradients are important, it is necessary to rebuild the local emission using inverse methods (Abel or Radon transform).

Chapter 4

Intensity Building

Once the broadened emission distribution $f_{Ar\&Ar^+}(\lambda, x, y)$ is obtained , the intensity distribution $I(\lambda, x, \theta)$ needs to be calculated and compared to the human eye sensitivity to rebuild the image of the plasma jet. In this section, the methods and principles explained in previous chapters are used to get closer to the final results.

The intensity was first calculated by means of the following expression:

$$I(\lambda, x) = \Delta x \sum_{y=y_{min}}^{y_{max}} f_{Ar\&Ar^+}(\lambda, x, y) \tag{4.1}$$

Where Δx is the spacial resolution along x.

However, this method would only be valid for planes of projection which are parallel to the original (x, y) axes, that is, angles of projection equal to 0° or 90° depending on the integrated dimension (x, y). Since it is interesting to obtain images at different projection angles, this method was discarded and the intensity of the emission is now calculated by means of the Radon Transform, as it has been previously explained.

This is done through the MATLAB function `radon`. In order to use this func-

tion, it is necessary to set another parameter which is the angle of the projection θ that is illustrated in figure 2.7. As it can be seen in the figure, θ determines the angle of the plane of projection x' with respect to the horizontal and initial axis x.

The input to this function is the broadened emission result ($f_{Ar\&Ar^+}(\lambda, x, y)$), which is a 2-D matrix for each z section, and the angle (θ). It is important to explain that `radon` admits angles from 0° to 179°, being 180° the same projection as 0°.

4.1 Human Eye Sensitivity

Once the intensity of the emissions is calculated, a filter is applied. In this case, the filter is the human eye. However, the developed tool lets the user apply any other intensity filters. Thus, the potential uses of this tool include the possibility to detect and build UV and IR radiation images, which provide sufficient information about the plasma jet to be able to select an appropriate camera among the set of sophisticated devices available in the market for experimental purposes.

The human eye sensitivity curves shown in figure 4.1 reflect that human beings are only able to capture electromagnetic waves with wavelengths between 400nm and 700nm approximately. Therefore, the final image will discard all the intensities existing over or below those wavelength limits. Furthermore, depending on the length of the electromagnetic wave, the human eye is able to see different colors. From 400nm to approximately 510nm, the human eye sees blue color, from 450nm to 650nm, the human eye sees green and from 550nm to 700nm the human eye sees red color. Those wavelength regions that correspond to several colors are the origin of the rest of the colors perceived by the human eye which are born by the mixture of Red, Green and Blue.

The intersection of the calculated intensity curves and the filter in figure 4.1 is

performed as follows:

$$I_{visible}(\lambda, x) = I(\lambda, x) \times I_{color}(\lambda) \tag{4.2}$$

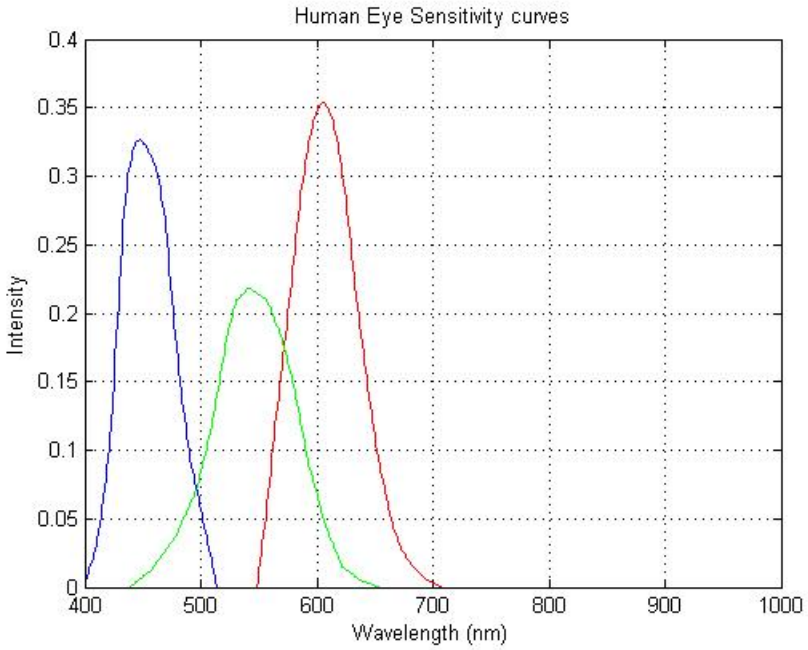

Figure 4.1: Human eye sensitivity curves

The graph shown in figure 4.1 has been digitalized. Therefore, just a few values of this function were obtained. Since to go for the next step it is necessary to evaluate the human eye intensity curves into the selected spectral grid, the MATLAB tool `fit` has been used. This tool creates a fit with the `fitType` specified. To obtain each curve in the most accurate way, the `fitType` `linearinterp` has been selected. This MATLAB function performs a linear interpolation resulting in the curves in figure 4.1.

The next step is to make the intersection between the intensity curves and the filter, in this case, the human eye intensity curves. Once the intensity is filtered by every color, the amount of each color per pixel is calculated by means of equation 4.3. Thus, given a z-position, the result of each sum is a vector that stores the

amount of red, green or blue projected at every x-position. Although it seems that this explanation is just for one section of the plasma jet, the tool performs a loop in MATLAB to obtain the amount of each color as well as every other data for all z-sections.

$$P_{color}(x) = \sum_{\lambda_0=\lambda_{min}}^{\lambda_{max}} I_{visible}(\lambda, x) \tag{4.3}$$

In this project, as it has been mentioned before, the values for λ_{min} and λ_{max} are $\lambda_{min} = 400nm$ and $\lambda_{max} = 1000nm$.

Given an x-position and a section z, the pixels in gray scale of x, z are obtained by adding together the pixels of each color at x, z as indicated in equation 4.4. Finally, the pixels are normalized to 1 (equation 4.5) by dividing every pixel by the maximum value of the pixels in gray scale $P_{B\&W,max}$ in the whole 2-D domain.

$$P_{B\&W}(x, z) = P_{red}(x, z) + P_{green}(x, z) + P_{blue}(x, z) \tag{4.4}$$

$$P_{color,normalized}(x, z) = \frac{P_{color}(x, z)}{max(P_{B\&W})} \tag{4.5}$$

The result of these last operations are three 2-D matrices, one for each color, with the fraction of each color in the (x, z) domain.

In MATLAB, as in other programming languages, the intensity color scale goes from 0 to 255 for every color. When the intensity of the three colors, that is, the value of the three red, green and blue pixels are below or equal to 0, there is no color, thus, the displayed color is black. Nevertheless, when the intensities

are above or equal to 255, then the displayed color is white. If the whole image is white, it is said to be saturated, therefore, it has to be adjusted. However, if just a few pixels are above 255, those pixels are said to be saturated although the rest of the image is not and the human eye can detect the corresponding colors.

By normalizing the intensities of the pixels, the tool stores the fraction of intensity with respect to the maximum (255) that has to be displayed for the image not to be saturated. Hence, by multiplying these fractions by the maximum, the exact color of the image is obtained.

$$P_{color,real}(x,z) = 255 \times P_{color,normalized}(x,z) \tag{4.6}$$

Finally, all the scaled intensity values are stored in a 3-D matrix that has to be converted into "unsigned 8-bit integers" as defined by MathWorks for the image to be represented correctly. To do so, `uint8` is used to obtain the input for the MATLAB function `imshow`, which displays the definitive images shown in the upcoming chapter.

Besides color images, black and white images can also be displayed using this tool if desired. The tool stores the sum of the color pixels as shown in 4.4. Thus, there is a black and while matrix at the end of the calculations available to be plotted. If the MATLAB function `imshow` receives as an input a 3-D matrix, it retrieves a color image in which the first dimension corresponds to the red color, the second, to the green and the third, to the blue, following the RGB pattern. Nevertheless, if the function receives a 2-D matrix as an input, it shows an image in gray scale. Hence, since the tool generates this 2-D matrix with black and white values, the image can be easily obtained.

Chapter 5

Assessment of the code

In this chapter, the outputs of the developed tool are shown and explained. Also, this chapter will focus on the source of the data that have been used to make the discussion about the results. The tool is versatile since it can base on any flow field and be able to provide the corresponding results taking into account that for each set of data, the output would be completely different.

5.1 Data acquisition

The tool created in this project has been tested by inputting a set of data that simulate real plasma jet cases. Nonetheless, as it has been previously explained, the tool can be used for any set of data desired by the user. For the acquisition of the results shown in upcoming sections of this chapter, two different sources of data have been used:

- **Spectroscopic Data:** First, there are a set of parameters that have been obtained from the National Institute of Standards and Technology (NIST) Atomic Spectra Database. These are:

  - The reference wavelength (λ_{ul}), which is the center of every spectral Gaussian corresponds to the maximum intensity at that specific wavelength.

  - The corresponding Einstein coefficient (A_{ul}), which is defined as the probability for an atom or molecule to emit light.
  - The energy in the upper level (E_u). This magnitude is the energy expressed in cm^{-1} that corresponds to the uppermost level involved in the electronic transition.
  - The degeneracy (g_u). This is the number of quantum states in the uppermost energy level of the transition.

- **Flow field definition:** Second, the data about the electron, neutral (Ar) and ion (Ar^+) temperatures and densities have been obtained from EP2PLUS simulations performed by Filippo Cichocki, member of the Aerospace Department at *Univeridad Carlos III de Madrid*. The results of these simulations have been plotted and shown in this report for a better understanding of the conditions. Two simulations have been performed:
  - The first one for a plasma jet with ordinary circular injection, the number of nodes in this simulation has been set equal to 101 for x, 101 for y and 151 for z. To make the flow antisymmetric, a cubic object has been placed in section Z=46 as it can be seen in table 5.3. The dimensions of this jet are 2m in x and y directions and 3m in z direction. Therefore, each Z,X,Y-nodes correspond to approximately 20mm in reality.
  - The second one for a plasma jet with annular injection, the number of nodes in this case has been set equal to 81 in x, 81 in y and 101 in z. Again to make the flow antisymmetric, an object has been placed in section Z=27, as it can be clearly seen in tables 5.1 and 5.2. The dimensions of the jet in this case are 2.5mm along x and y directions and 1cm along z direction. Therefore, each Z-node corresponds to 0.1mm in reality and each X,Y-node correspond to approximately 0.03mm in reality.

In the tables 5.1, 5.2 and 5.3, the particle and temperature distribution of the simulated cases are shown. In the case of annular injection, a wider set of data were

Node	$Z = 10$	$Z = 27$	$Z = 70$
$N(Ar)$	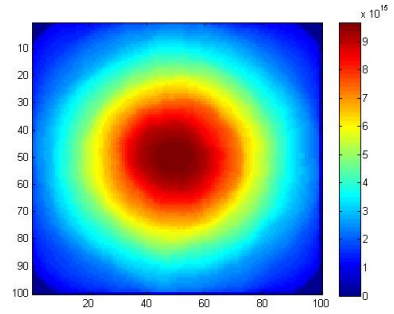	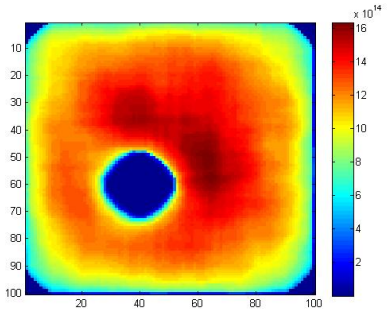	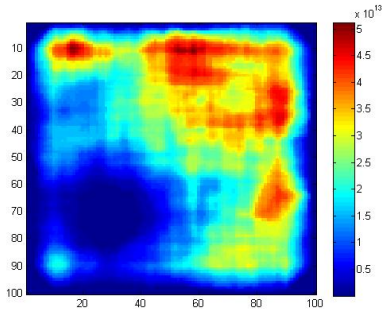
$T(Ar)$	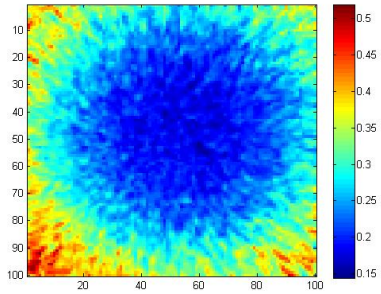	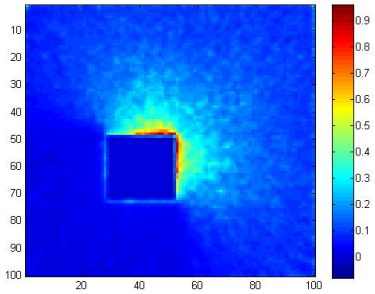	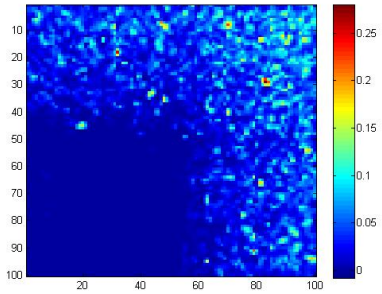

Table 5.1: Plasma jet for annular injection. Plots of the neutral densities and temperatures for a set of cross sections

extracted from the simulation, However, in the case of ordinary circular injection and for the sake of simplicity, only the data for ions (Ar^+), have been extracted from the simulation. Hence, the temperature distribution has been considered the same in both cases and density distribution of neutrals have been assumed to follow equation 5.1.

$$\frac{N_{Ar}}{N_{Ar^+}} = K \tag{5.1}$$

Where K is a constant that has been set to different values in order to consider the case of highly ionized and low ionized plasma.

Node	$Z = 10$	$Z = 27$	$Z = 70$
$N(Ar^+)$	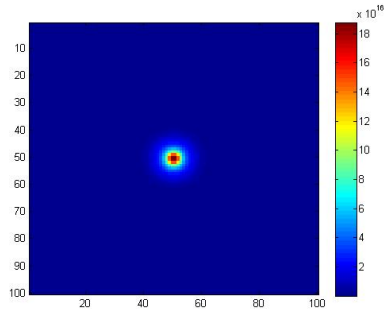	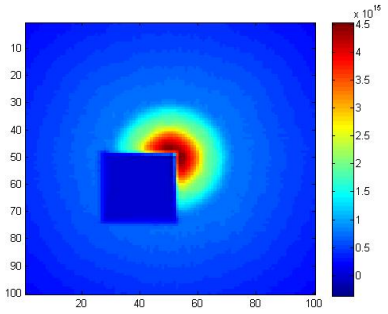	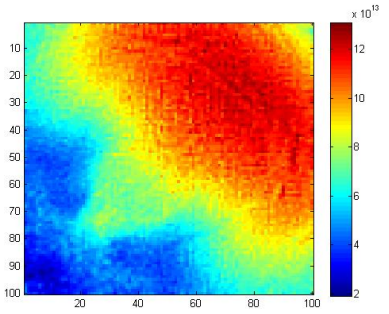
$T(Ar^+)$	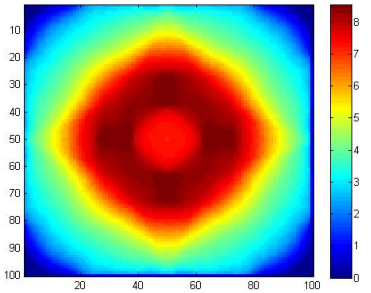	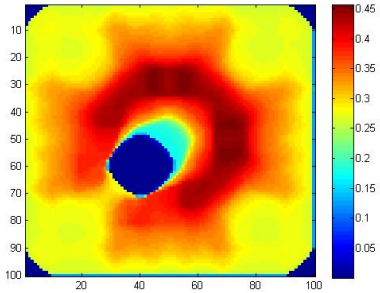	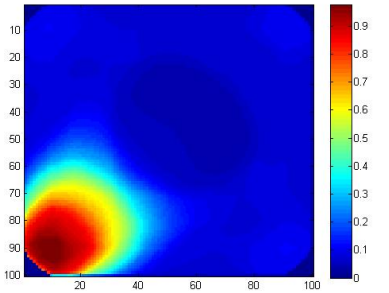
$T(e^-)$	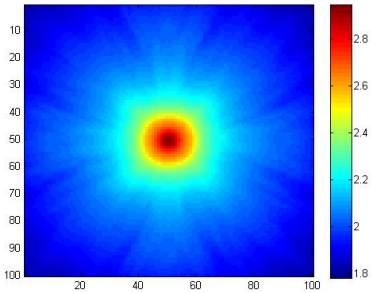	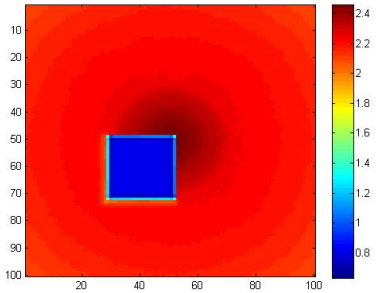	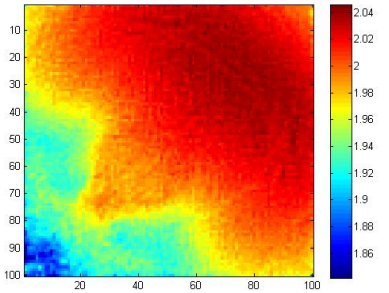

Table 5.2: Plasma jet for annular injection. Plots of the ion densities and electron and ion temperatures for a set of cross sections

Since the process of oscillations is assumed to be dominated by electronic inelastic collisions, it can be said that $T_{ex} \approx T_{e^-}$. While the electron temperature has been calculated using relationship 5.2.

Node	$Z = 10$	$Z = 46$	$Z = 70$
$N(Ar^+)$	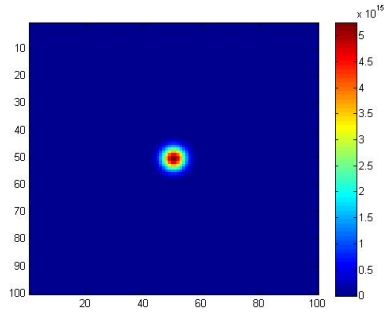	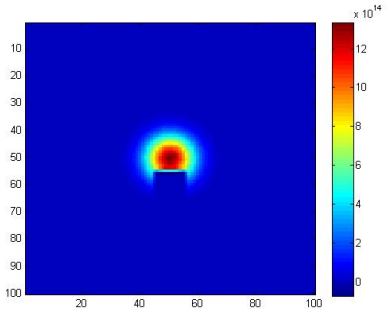	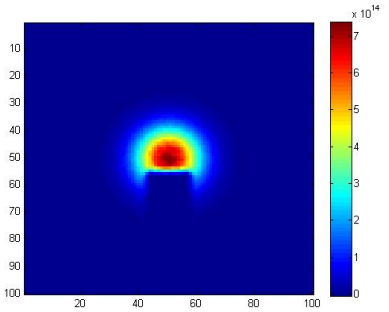
$T(Ar^+)$	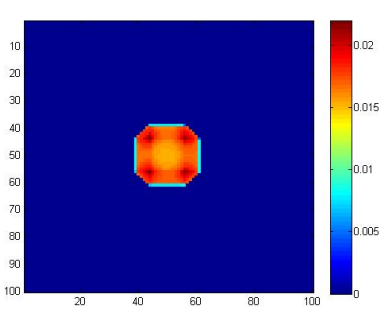	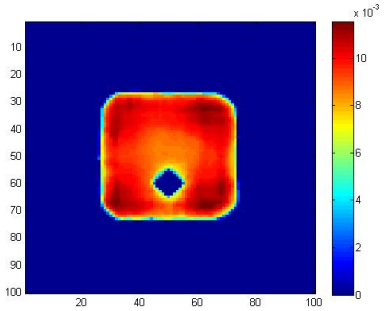	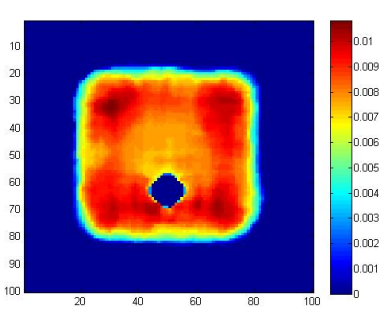

Table 5.3: Plasma jet for circular injection. Plots of the ion densities and temperatures for a set of cross sections

$$\frac{T_{e^-}}{T_{e^-,0}} = \left(\frac{N_{e^-}}{N_{e^-,0}}\right)^{\gamma-1} \tag{5.2}$$

Where $\gamma = 1.05$ and N_{e^-} is the electron density obtained from [14].

In tables 5.1 and 5.2 for the annular injection case, the density of ions is higher than the density of neutrals in the center of the plasma jet. This does not mean that there are more ionized particles than neutrals but that the ionized particles are concentrated in the center of the section since they travel at a higher velocity as it can be inferred from the temperature distributions in the same tables. Since ions and electrons are charged particles, they experience changing attractive and repulsive forces that make them travel at higher speeds, resulting in a higher tem-

perature in the center of the section. Moreover, it can be clearly seen that neutrals deviate from the jet trajectory more easily than ions.

If tables 5.1 and 5.3 are compared, it can be seen that the annular injection contributes to the dispersion of neutrals in space and also, that the presence of an object causes more disturbances the closer to the plasma injection since upstream particles are more energized. In the ordinary circular injection case, the distribution of particles and temperature is really stable in comparison to the annular case.

5.2 Emission Results

The aim of this section is to show and discuss the results obtained throughout the calculation process. As explained in previous chapters, the Ar and Ar^+ spectra are first obtained separately. From this step, valuable information can be obtained which will be crucial for the image analysis.

Figures 5.1a and 5.1b are the result of equations 3.9 and 3.10 for the ordinary circular injection case. In those figures it can be seen that Ar^+ most significant emission lines are concentrated at the left part of the spectral grid, this part corresponds to low wavelength values. In contrast, Ar emission lines are concentrated in the right part of the spectral grid, having higher wavelengths and lower frequencies. As the energy is proportional to the frequency according to equation 2.2, it can be concluded that Ar^+ emissions are more energetic than Ar emissions.

Moreover, it can be seen that the emission peaks reached in figure 5.1a are much higher in value than the peaks in figure 5.1b. This can be explained by having a look at equation 5.1. Depending on the particle distribution and since the emission is directly proportional to the particle density per unit volume, the emission peak values will depend on the value of the constant K in that expression. However, since there is no physical point on setting the constant $K < 1$, the peak values of Ar local emission will be always higher than the peak values of Ar^+ local

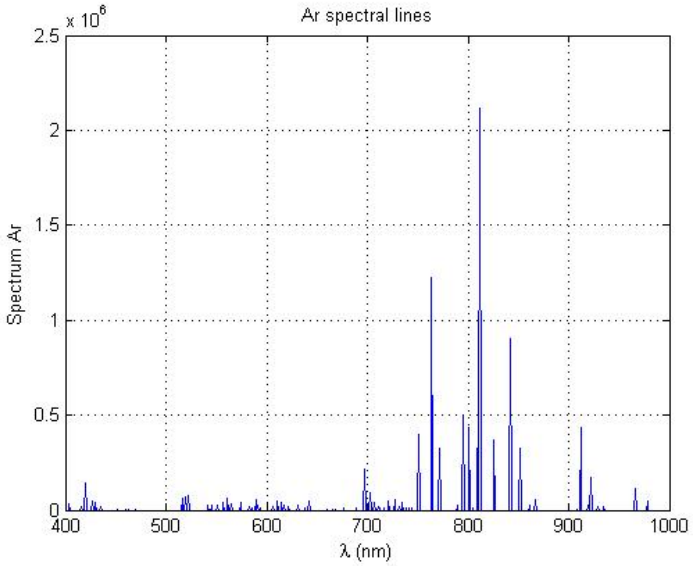

(a) Ar

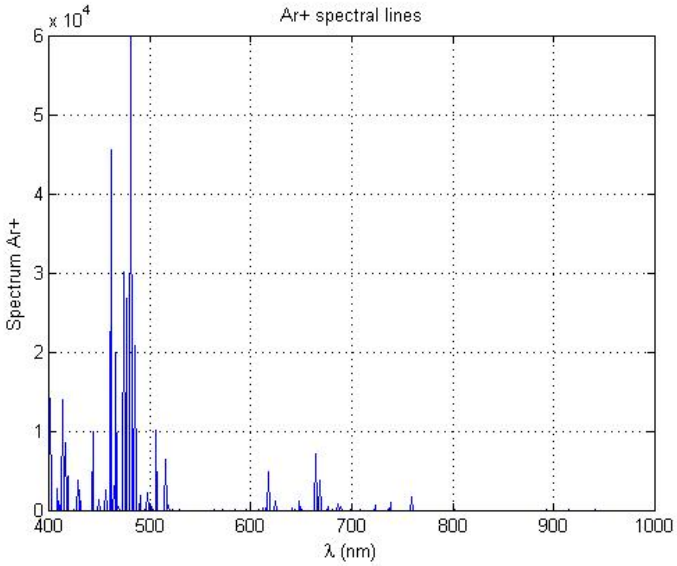

(b) Ar^+

Figure 5.1: Ar and Ar^+ central emission spectra at Z=10 for ordinary circular injection jet

emission for the ordinary circular jet case.

Nevertheless, in the case of annular injection, since the density distributions have been directly obtained from the simulations, there are some unit volumes in which the density of ions is higher than the density of neutrals, although this does not mean that there are more ions than neutrals in the whole volume. The result of this is the presence of higher peak values in the local emission of Ar^+ than in the one of Ar for some specific spacial points although the contrary case also takes place at certain unit volumes. This can be appreciated in figures 5.2a and 5.2b.

Once the particular emission graphs have been obtained, they are put together to have the whole emission spectrum, as explained in previous chapters. Although there are as many spectral graphs as unit volumes in the simulated plasma jet, a few of them have been plotted and plugged in this report.

Figures 5.3a and 5.3b show the spectra of Ar and Ar^+ at certain values of x, y, and z. In these three cases, $x = 50$, $y = 50$ and the values for z-section can be observed in each graph. In those figures, the number of spectral lines is the

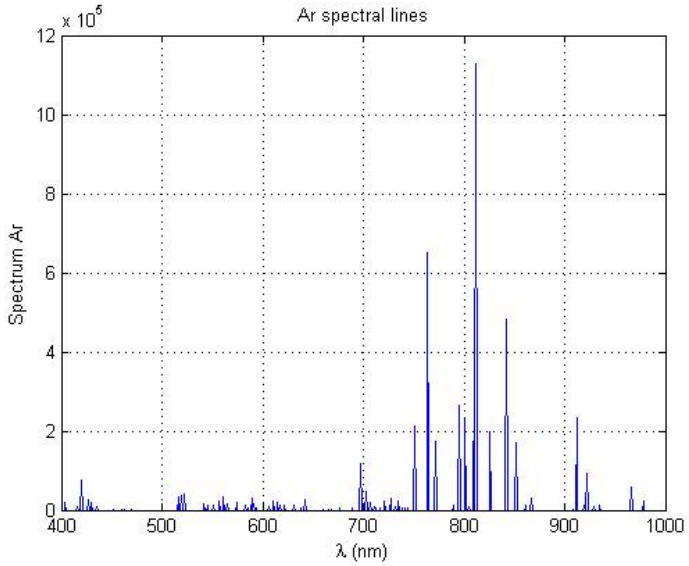

(a) Ar

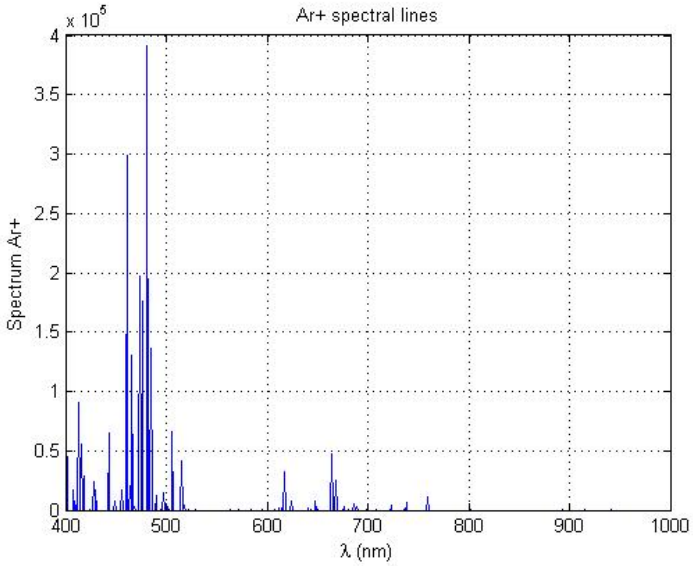

(b) Ar^+

Figure 5.2: Ar and Ar^+ central emission spectra at Z=10 for annular injection jet

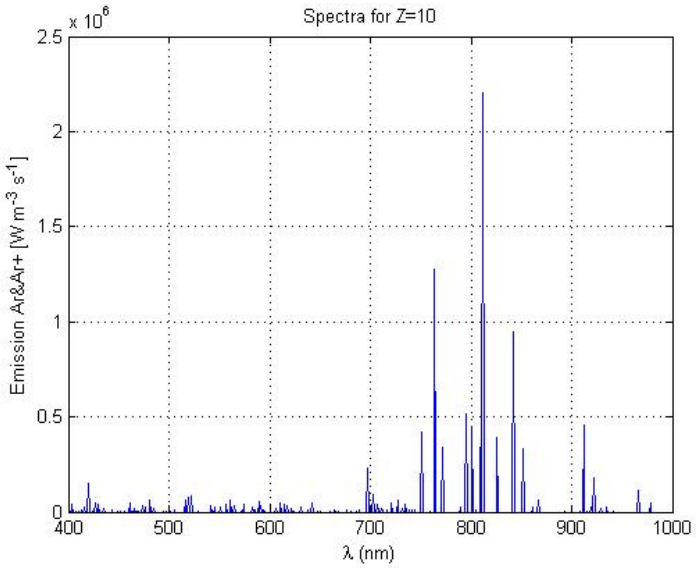

(a) Z=10

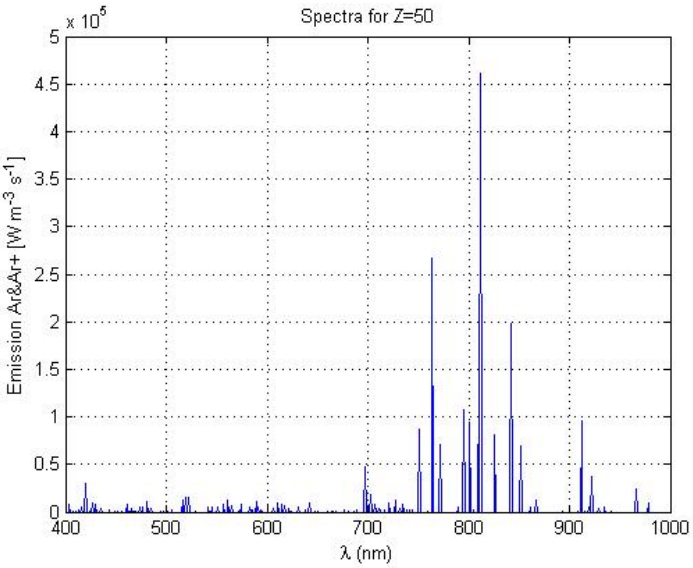

(b) Z=50

Figure 5.3: Spectra of Ar and Ar^+ in the center of the plasma jet for circular injection

same and it comes from the NIST Atomic Spectral Database. However, the graphs show that the emission is not the same on every point. Instead, they depend on the local temperature and density distributions, which make the emission profiles change when the x, y, z position varies.

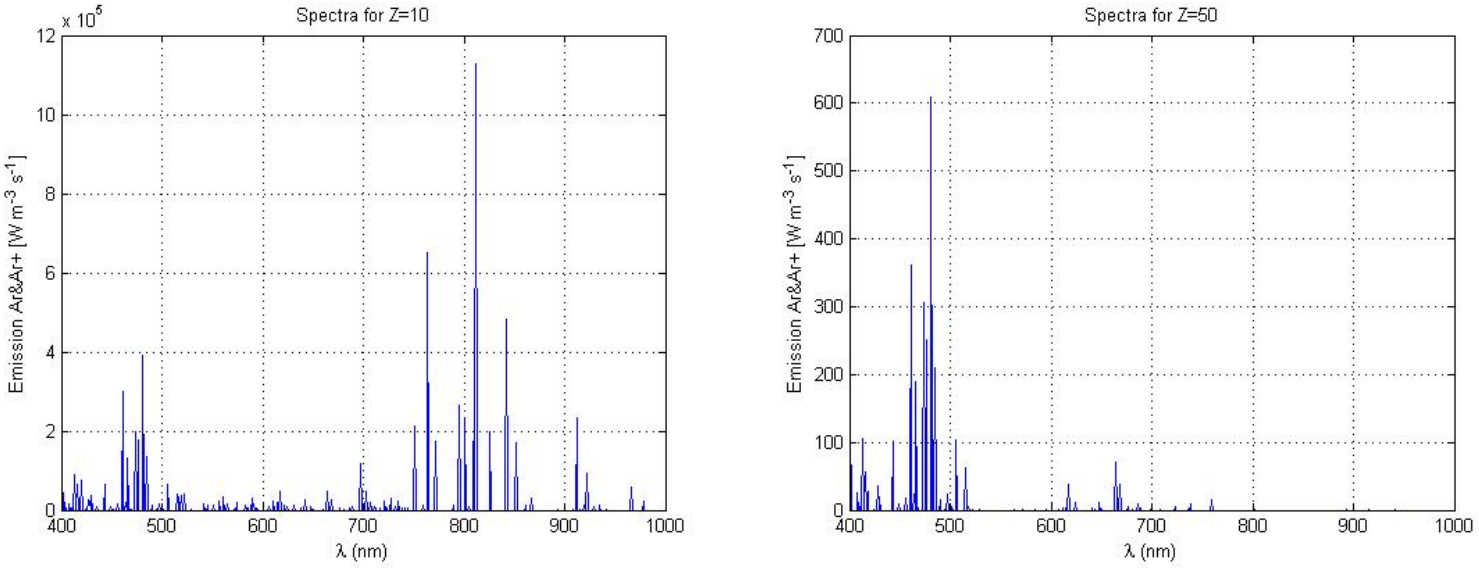

(a) Z=10 (b) Z=50

Figure 5.4: Spectra of Ar and Ar^+ in the center of the plasma jet for annular injection

The spectra have been intentionally selected at the center of the jet due to the density and temperature profiles of the simulation. As it can be seen in table 5.3, since the temperature is the result of the velocity of particles, it depends on the density distribution. As it has been appreciated in the representation of the input data, the temperature and the density become lower the further from the center. Therefore, the spectral lines will be smaller at an x, y position different from the center and there will be no spectral lines in the edges of the simulation due to the absence of particles in that region.

It is possible to tell the difference between both the ordinary circular and the annular injection simulations by just having a look at the emission spectra plotted in figures 5.3a, 5.3b, 5.4a and 5.4b.

- In the ordinary circular injection case, the particles spread over a higher circular area at sections further from the origin as it can be seen in table 5.3. This effect makes the total particle density decrease in the center of the jet and also does the electron temperature for sections located far from

the origin. If these reductions are evaluated in equations 3.1 and 3.2, the reduction of the electron temperature clearly makes the exponential decrease, which together with the density reduction, make $N_{u,Ar}$ and N_{u,Ar^+} decrease. Since this value is directly proportional to the emission, the emission values at Z=10 are higher than those at Z=50. Also it is important to consider that there is antisymmetric behavior due to the presence of an object in the jet, which affects the local emission at certain unit volumes.

- In the annular injection case, the presence of an object disturbs the flow in a significant way such that the flow is non symmetric downstream from the object. Therefore, after the object there are some z-sections at which there is no emission at all, since the particle density is zero. Furthermore, there are some other regions where the neutral density is zero but there is presence of ions and vice versa. This is the case of Z=50 that is plotted in figure 5.4b. In this section there is presence of Ar^+ but there are not Ar particles, this will result in a blue color in this section of the plasma jet.

The sharp spectral lines in figures 5.3a and 5.3b can be smoother and better defined when the spectral resolution is increased. In order to modify the spectral resolution, the so-called $\Delta grid$ parameter that was previously set to 1nm has to be decreased. Focusing on one specific Gaussian, the effects of the spectral resolution can be observed in figure 5.4. The lower the increment ($\Delta grid$), the higher the spectral resolution and the more accurate the results for the local emission. Figure 5.4 shows the evolution of a spectral line centered at $\lambda_{ul} = 812nm$ for two different z-positions and for x and y positions equal to 50, that is, the center of the plasma jet. It can be seen that for a $\Delta grid$ equal to 0.0001nm the spectral line is a Gaussian as expected. However, for simplicity and to save computational time, $\Delta grid$ has been used as 1nm in the rest of the project.

$\Delta grid$	$Z = 10$	$Z = 50$
$1nm$	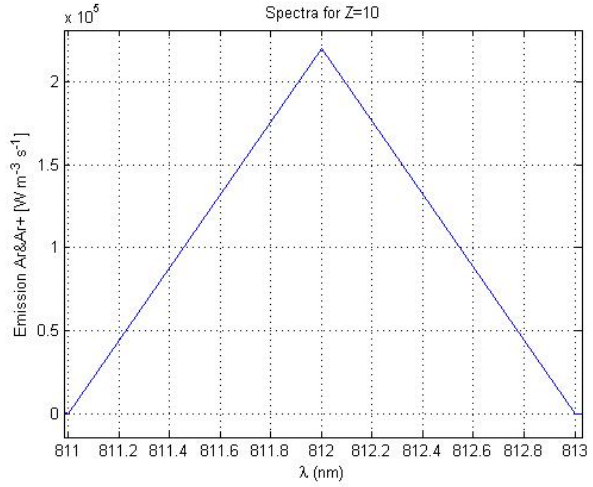	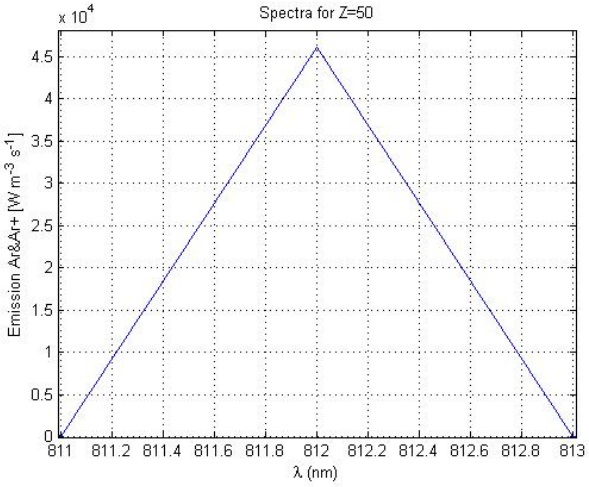
$0.001nm$	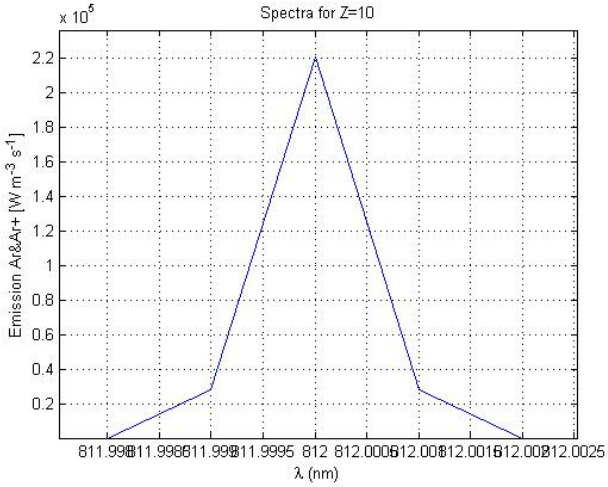	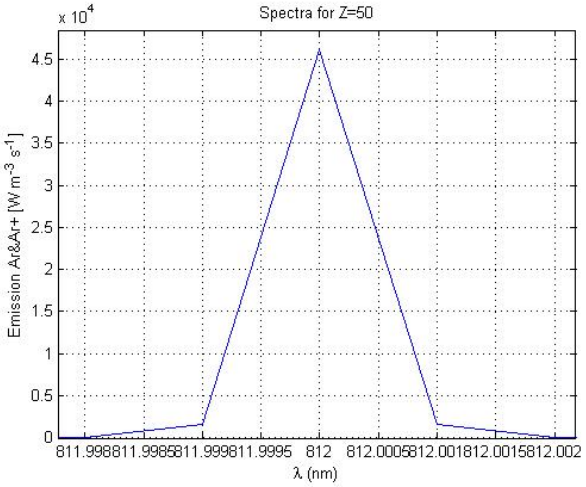
$0.0001nm$	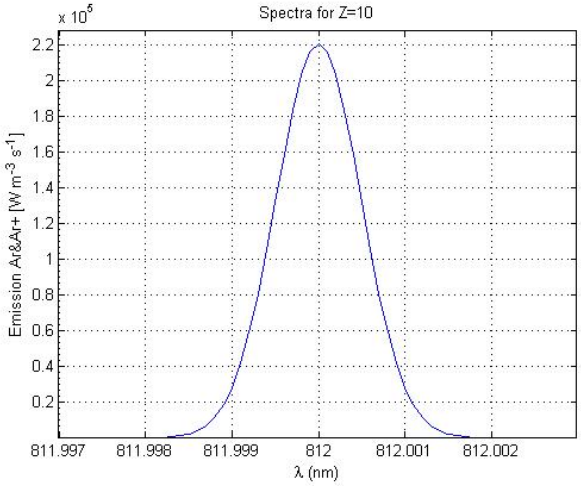	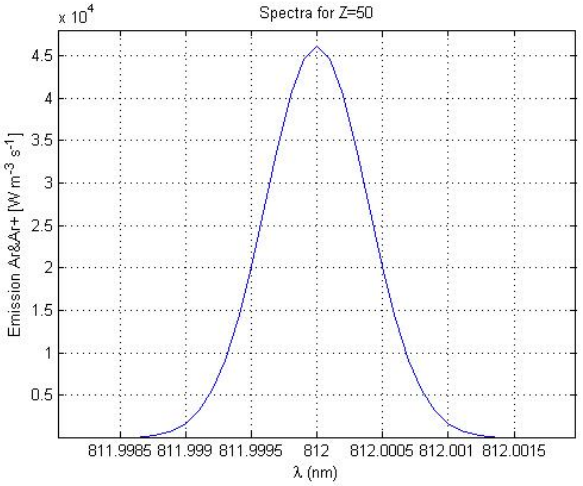

Table 5.4: Effect of the spectral resolution on the $\lambda_{ul} = 812nm$ line

5.3 Plasma spectra intensity: Temperature results

In order to characterize the plasma flow, two spectral lines with sufficient difference in internal energies have been selected to calculate the slope of the Boltzmann plot as explained in previous chapters. These lines are the following:

λ_{ul} [nm]	$A_{ul}[s^{-1}]$	$E_u[cm^{-1}]$	g_u
675	$1.93 \cdot 10^6$	118906	5
764	$2.45 \cdot 10^7$	106237	5

Table 5.5: Data of the spectral lines selected for the characterization

Since in this project, the emission distribution over the whole volume is available because the primary data come from computer simulations, it is possible to calculate the local temperature at the center of the plasma jet. However, from the experimental point of view, the emission distribution will be never available locally in the jet but just the projection of this emission.

Depending on the intensity profile of the plasma jet it is possible to derive the temperature at a certain unit volume of the jet. In this section, the temperature for both, the annular and the ordinary injection cases will be derived using the method explained in the previous chapters.

First, the temperature is calculated at the center of the plasma jet for a height of Z=10 for both the ordinary circular and for the annular injection cases.

Then, the temperature is derived for the projection of the emission profiles, this is the calculation with experimental interest, since during the laboratory tests it is not possible to have access to the center of the plasma jet.

As shown in table 5.6 in the case of ordinary circular injection, the excitation temperature calculated using the projected emission at the center is very similar

	SIMULATION	CALCULATION	
Type of injection	$T_{ex,center}[K]$	$T_{ex,center}[K]$	$T_{ex,projection}[K]$
Ordinary circular jet	33794	33794	33125
Annular jet	34039	34039	28955

Table 5.6: Excitation temperatures at Z=10 for two types of plasma injection

to the real temperature at the center of the plasma jet since the projected emission lines are very similar to the emission at the center of the jet. This is due to the shape of the injection, for this type of plasma jet, the location of the maximum excitation temperature coincides with that of the maximum particle density. Therefore, the temperature of the projection is very close to the maximum temperature.

In the case of annular injection, the projected emission has higher peaks than the emission at the center, due to the particle density distribution. Since the excitation temperature decreases when the emission increases, the excitation temperature derived by this method is lower than the temperature at the center of the plasma jet. Unfortunately, from just this characterization it is not possible to determine to which specific section of the plasma jet the temperature corresponds.

Figure 5.5b shows the emission profile at the center of the ordinary injection plasma jet, this profile can be approximated as a rectangle, therefore, the temperature derived using Boltzmann plot for the projected emission is very similar to the real temperature at the center. However, as it can be seen in figure 5.5a, the emission profile for annular injection cannot be approximated. Thus, the temperature derived corresponds to some unit volume but it is not possible to deduce where using this method.

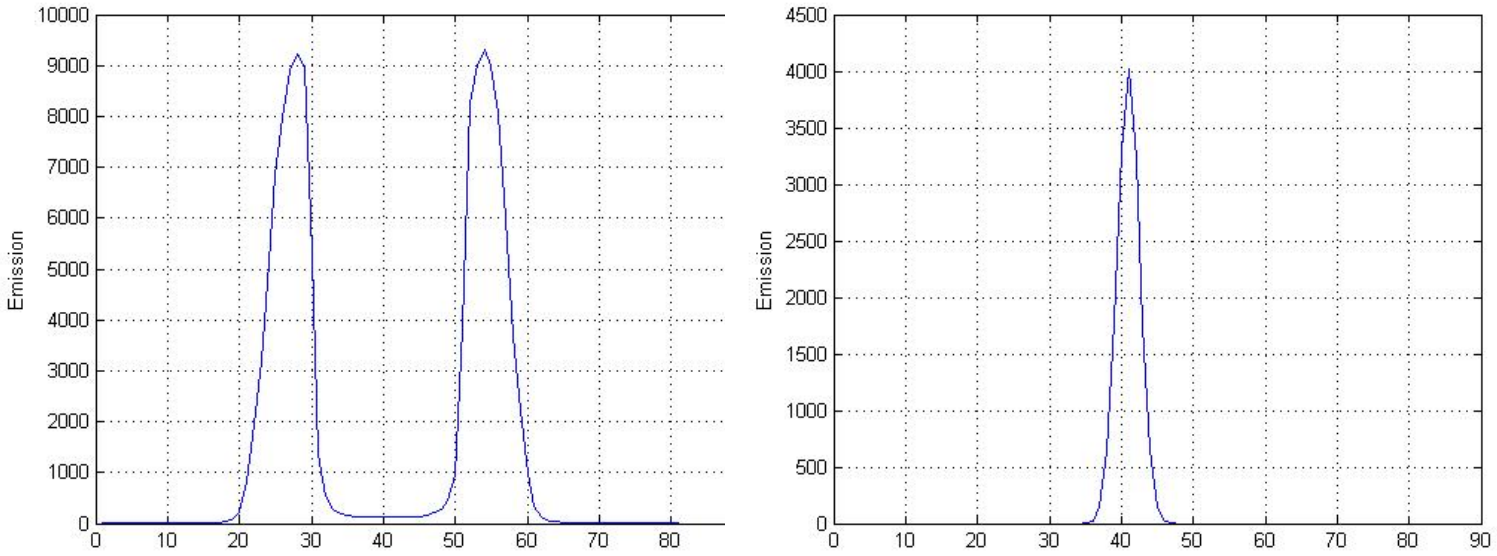

(a) Annular injection case

(b) Circular injection case

Figure 5.5: Emission profiles at the center of the plasma jet for Z=1

5.4 Intensity results

In this project, since there is an object in a side of the plasma jet trajectory in both the circular and the annular injection cases, different values of θ have been set in order to see the asymmetries of the jet in the resulting images and be able to analyze them.

In order to illustrate the calculations and show the intensity results, figures 5.6a, 5.6b, 5.7a and 5.7b show the intensity profiles for the mid point of the plasma jet at Z=10 and Z=50 in order to see the difference with the emission profiles shown in figures 5.3a, 5.3b, 5.4a and 5.7b.

These intensity profiles are very similar in shape to the emission profiles in most cases since they are just an orthogonal projection of the emission curves. Nevertheless, it can be seen that there are some important differences in the case of figures 5.4b and 5.7b. Due to the asymmetries coming from the presence of an object, the intensity profiles after the object and the emission profiles do not look alike.

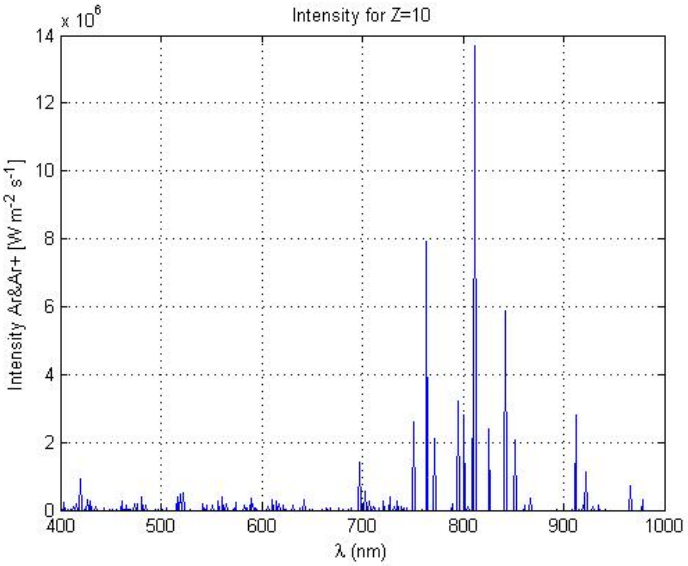

(a) Z=10

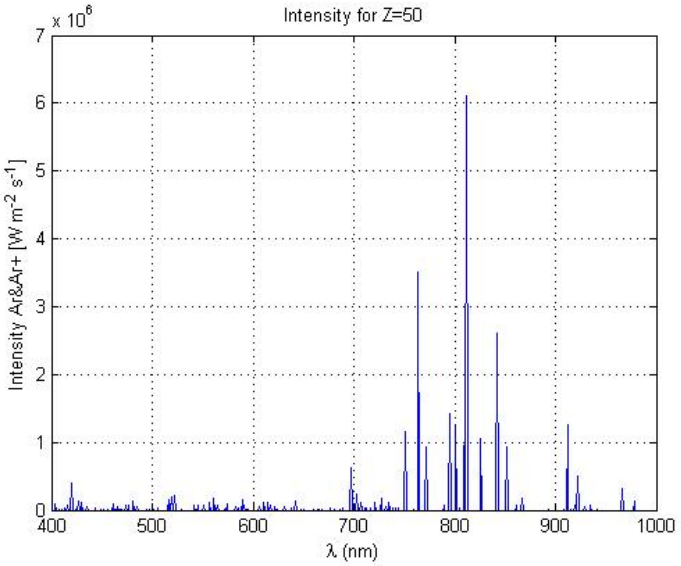

(b) Z=50

Figure 5.6: Intensity of Ar and Ar^+ in the central projection of the plasma jet $\theta = 90°$ for ordinary circular injection

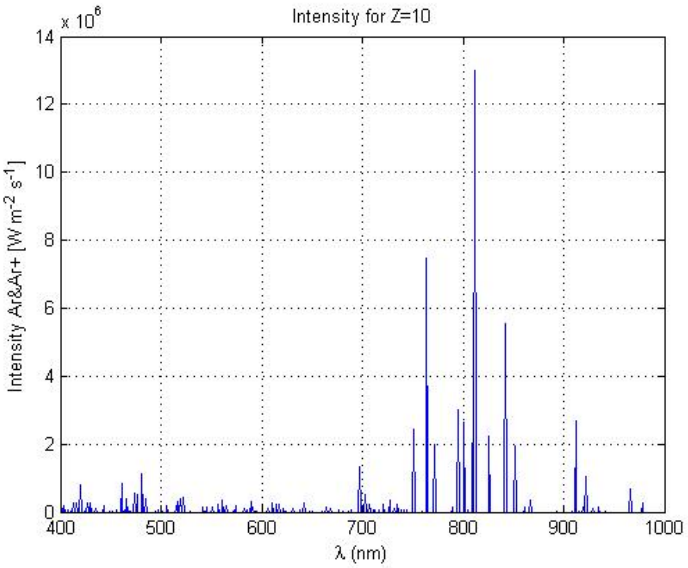

(a) Z=10

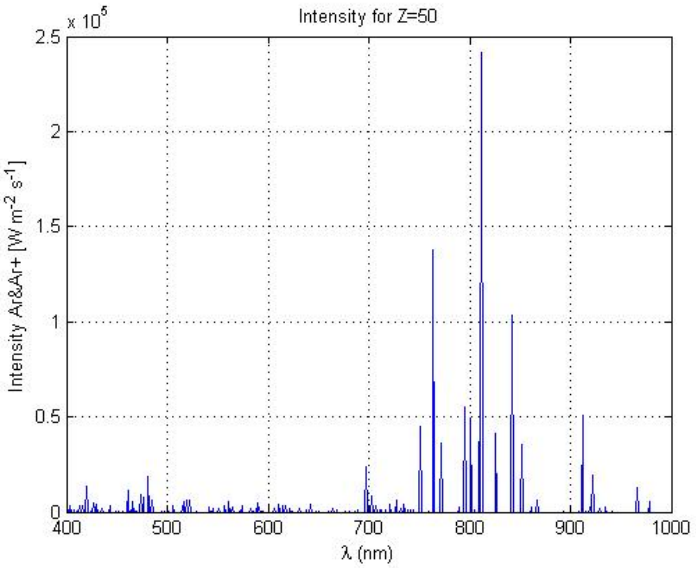

(b) Z=50

Figure 5.7: Intensity of Ar and Ar^+ in the central projection of the plasma jet at $\theta = 90°$ for annular injection

For the z-positions upstream of the object, the maximum emission location can be deduced due to the symmetry of the profile. Nonetheless, downstream of the object, the spectrum with the highest emission can be located anywhere. Therefore,

the projected emission is different from the emission at the center of the x, y plane.

As explained in previous chapters, once the intensity spectra are obtained, they are filtered with the human eye sensitivity curves shown in figure 4.1. Then, taking into account the spectral position of the colors seen by the human eye, it is possible to establish an analogy between the human eye intensity curves and the emission lines of Ar and Ar^+. The leftmost part of the spectral lines correspond to the Ar^+ spectral lines, as explained in the previous section. Therefore, these lines will be responsible for blue light. For the same reason, Ar emission will be responsible for red light according to the human eye sensitivity curves shown in figure 4.1.

The intersection is carried out according to equation 4.2 and the results are shown in figures 5.8a, 5.8b and 5.8c.

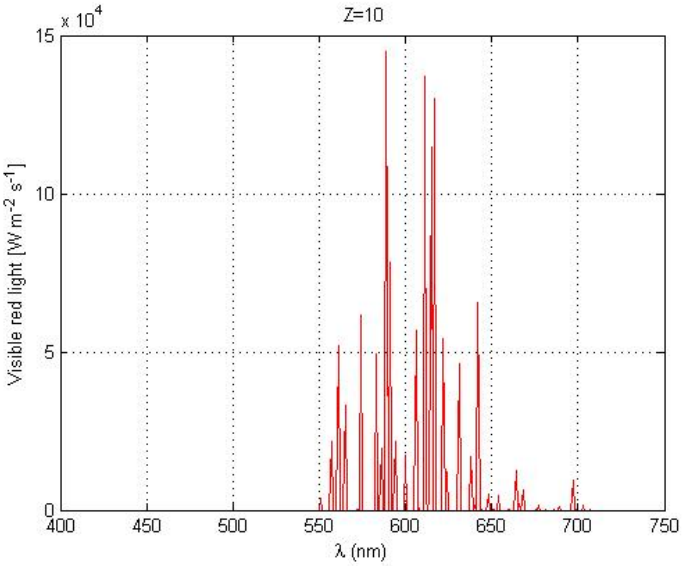

(a) Red Light

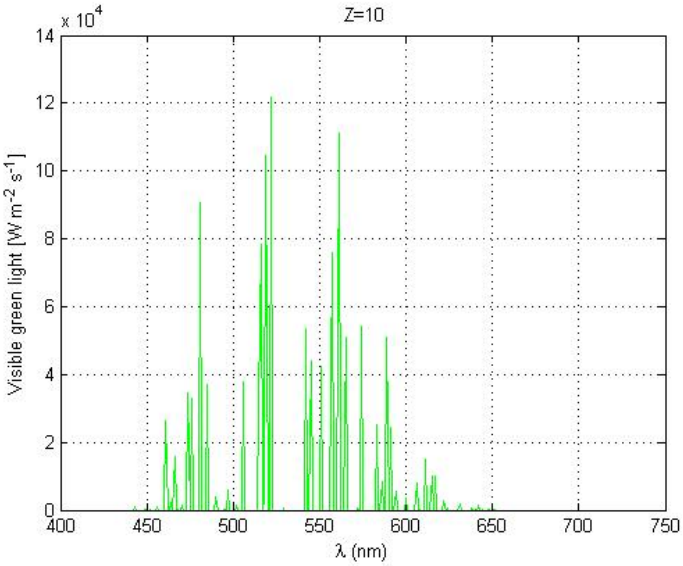

(b) Green Light

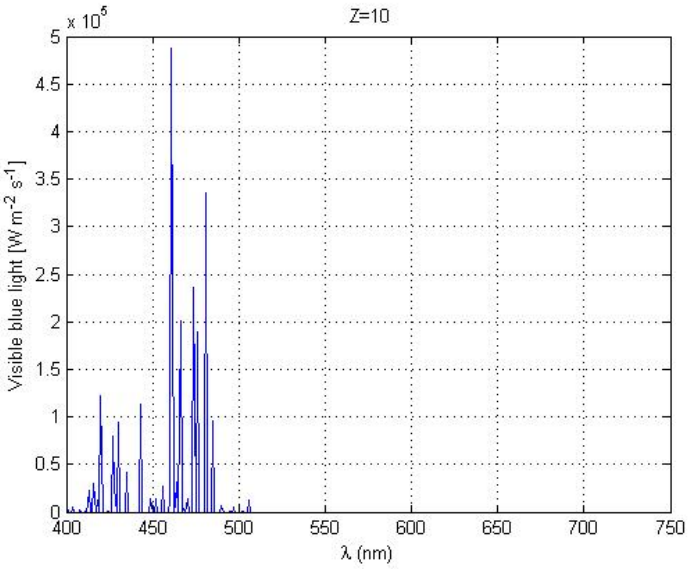

(c) Blue Light

Figure 5.8: Filtered intensities: Red, Green and Blue at Z=10

5.5 Image Results

This section focuses on physically analyzing the image output of the code. For a better analysis of the two simulated plasma jets, several angles have been chosen to obtain a set of views of the jet for each simulation.

Although the images have been scaled as explained in the previous chapter to

avoid image saturation, the resulting images are really dark. Therefore, although this means that there are some saturated pixels, these have been multiplied by a factor of 1000 in the ordinary circular case and 500 for the annular case instead of 255 in order to be able to see the plasma jet in a clearer way.

The tool has been run for $\theta = 0°$, $\theta = 45°$, $\theta = 90°$ and $\theta = 135°$ in order to have a wide set of views of the plasma jets in both simulations. The images obtained can be seen in figures 5.9a, 5.9b, 5.9d and 5.11b for the case of annular injection and figures 5.13a, 5.13b, 5.13c and 5.13d for the case of circular injection. In order to analyze the jet in a better way, in the annular case, 50 out of the 100 z-nodes have been represented in the pictures, thus, it correspond to 5mm in z and 2.5mm in x directions. In the circular case, 100 out of the 151 possible z-nodes have been represented in the images, which corresponds to a plasma jet of 2x2x2m, resulting in 2x2m pictures.

-Annular injection

In the case of annular injection, figure 5.10a shows a dark white or even yellow color at the first stages of the plasma jet. This color is the result of the mixture of the three colors, in different proportions, which can be physically interpreted as a presence of both Ar and Ar^+ particles in those sections as it can be seen in figures 5.10b and 5.10c. However, once the maximum ion temperature point is reached (which is the point in which all the particles collapse) the jet becomes blue. The blue color is normally associated to the Ar^+ particles. Therefore, since more energy is concentrated in that point, the number of ionized particles increases in that unit volume, while the Ar particles spread, changing the color of the jet to blue. In figure 5.10b it can be seen that the blue color displayed in the jet matches those regions with presence of Ar^+ and absence of Ar. Also, figures 5.11a and 5.11b have been squeezed in order to better analyze the behavior of the jet when colliding with the object. It can be appreciated that the color changes to black at a certain section that is Z=27. Moreover, the blue color turns white just before the object, this is due to the fact that when colliding with the object, the ions

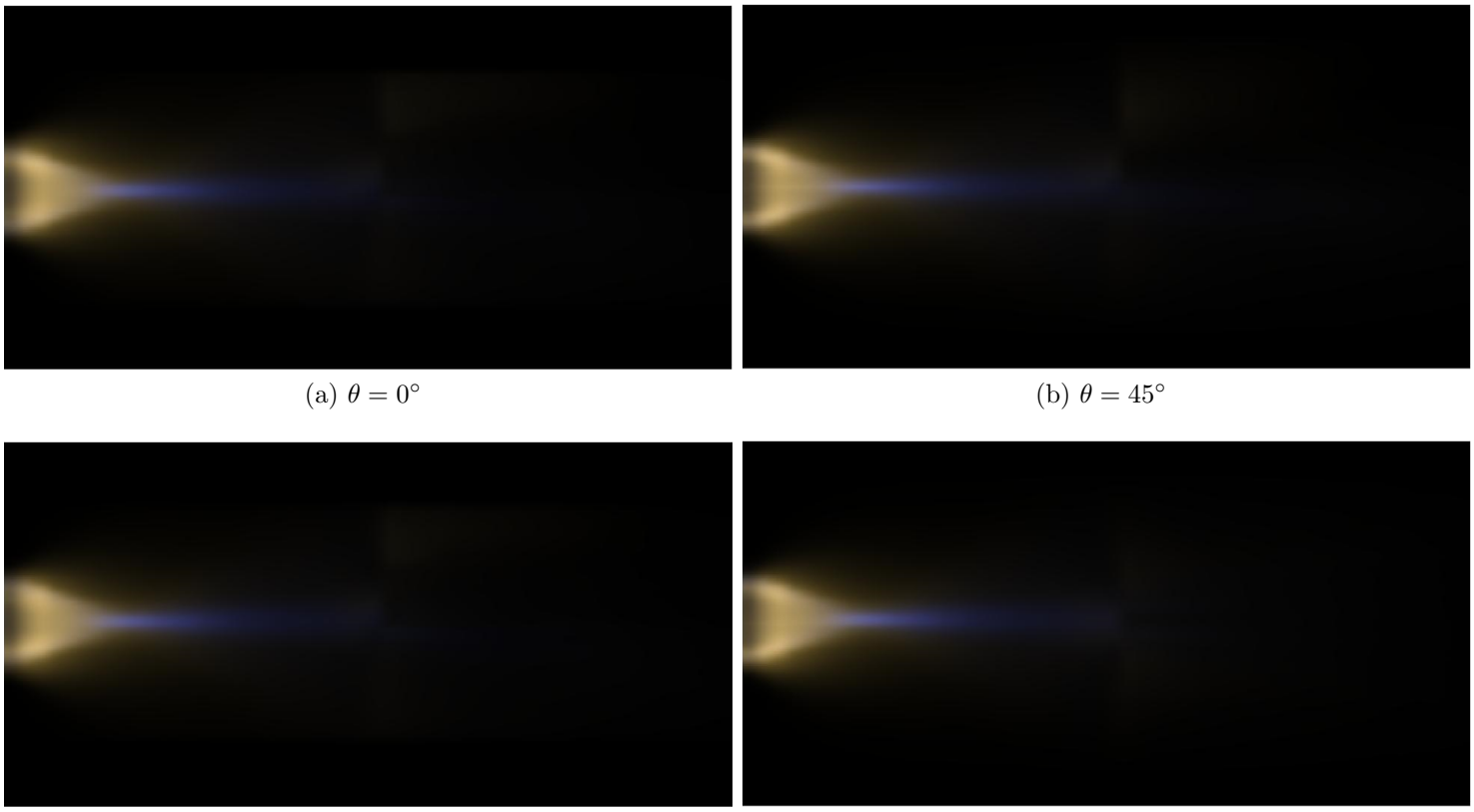

(a) $\theta = 0°$ (b) $\theta = 45°$

(c) $\theta = 90°$ (d) $\theta = 135°$

Figure 5.9: Final scaled images for annular plasma injection

bounce as neutrals. Increasing the Ar concentration in that section and changing the colors seen in the image, which can also be seen in the Ar particle density graph shown in figure 5.10c.

Furthermore, it can be appreciated that the views change with the angle of the plane of projection. The main difference can be observed between $\theta = 135\circ$ and the other three angles, in figure 5.11b, the object seems to cut the entire jet. However, in figure 5.11a, it can be seen that the object is interrupting just a piece of the jet trajectory.

(a) Plasma jet

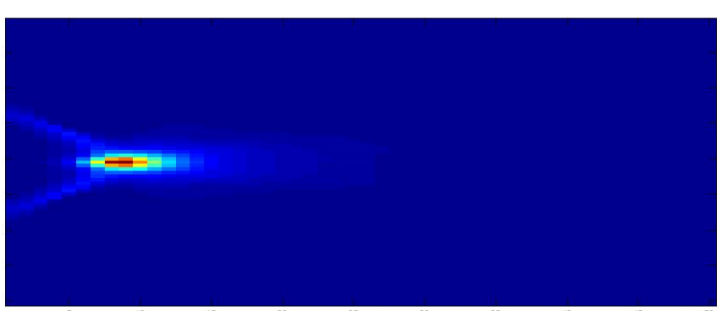

(b) N_{Ar^+} distribution

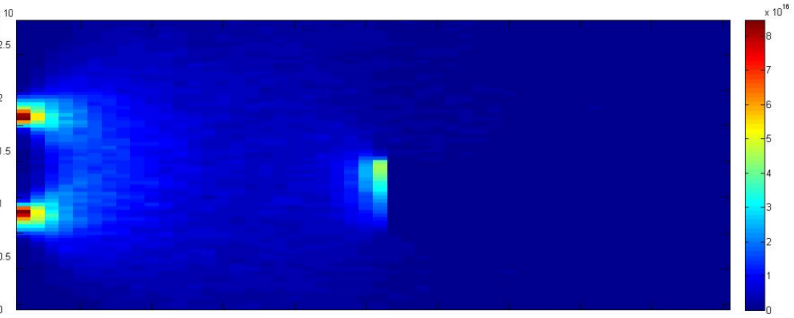

(c) N_{Ar} distribution

Figure 5.10: Ar and Ar^+ distribution in the annular plasma jet

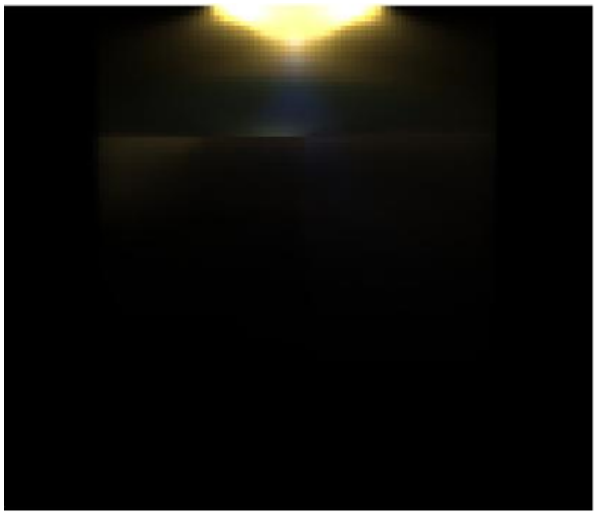

(a) $\theta = 90°$

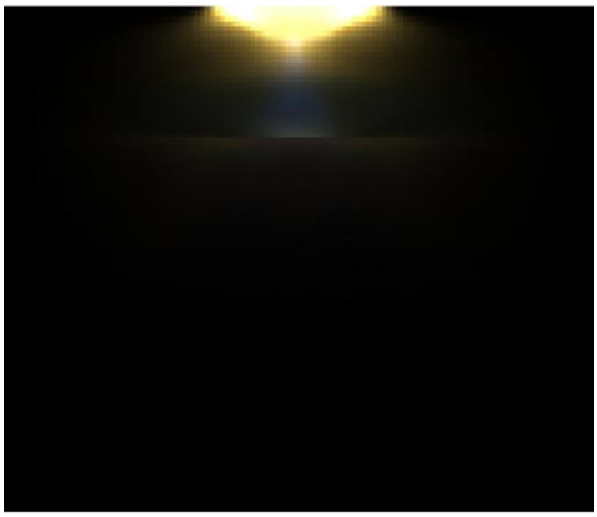

(b) $\theta = 135°$

Figure 5.11: Final images for annular plasma injection (not scaled)

-**Ordinary circular injection**

In the case of ordinary circular injection plasma jet, two different ion concentrations have been used in order to analyze the color variation. First, the factor K

described in equation 5.1 has been set to $K = 2$. Therefore, in this case the flow is highly ionized and the jet color tends to blue due to the high concentration of ions as it can be seen in figure 5.12a. In the second case, the factor K has been set equal to $K = 50$ and the obtained jet tends to orange, as a result of the mixture of green and red. The result is shown in figure 5.12b.

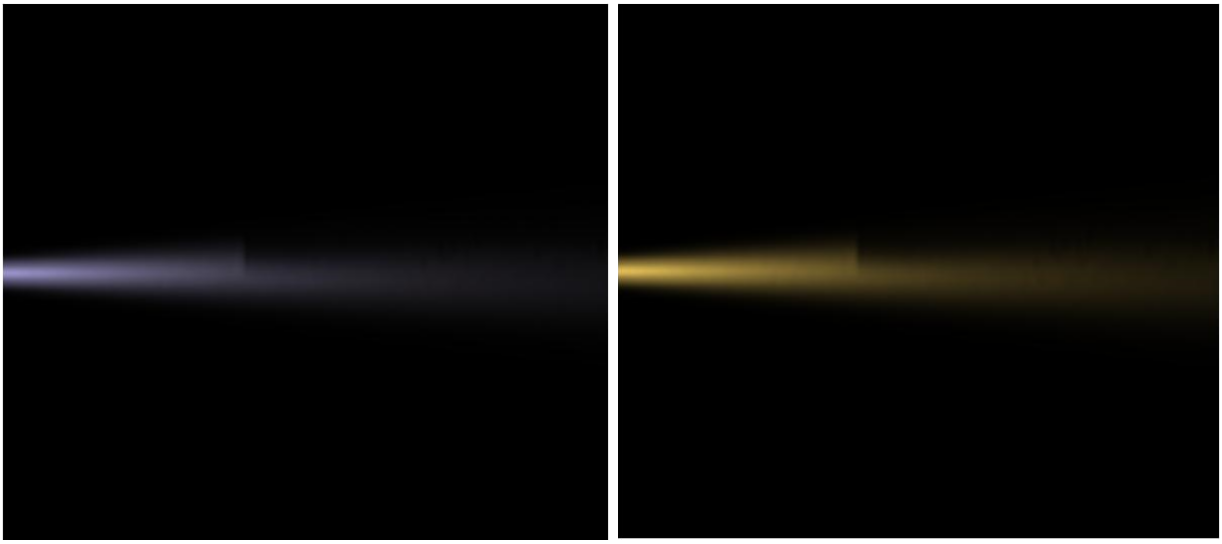

(a) $K = 2$ (b) $K = 50$

Figure 5.12: Highly ionized (a) vs. Low ionized (b) ordinary circular injection plasma jet

However, since the density distributions are the same but for the concentration of particles, in this case there are no regions with absence of the other specie. Therefore, the most interesting part of this simulation is to see the images from a different view reference as they can be observed in figures 5.13a, 5.13b, 5.13c and 5.13d. In those figures, the object in the jet trajectory can be clearly seen in a different position depending on the angle of projection.

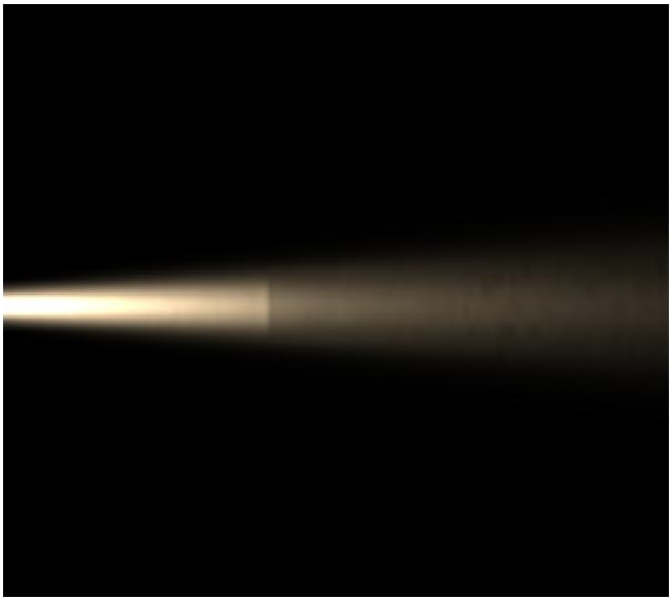

(a) $\theta = 0°$

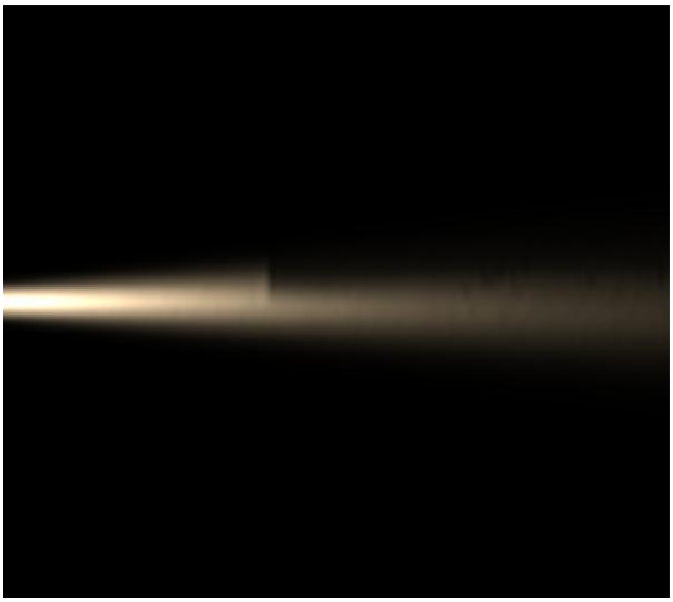

(b) $\theta = 45°$

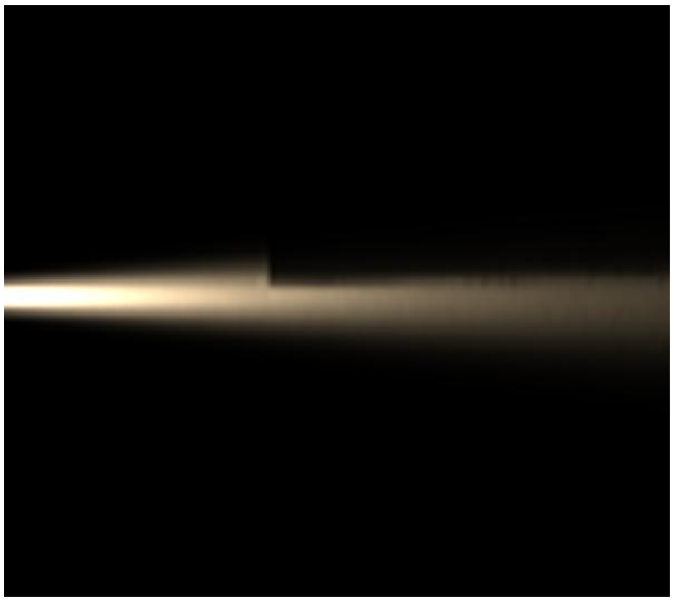

(c) $\theta = 90°$

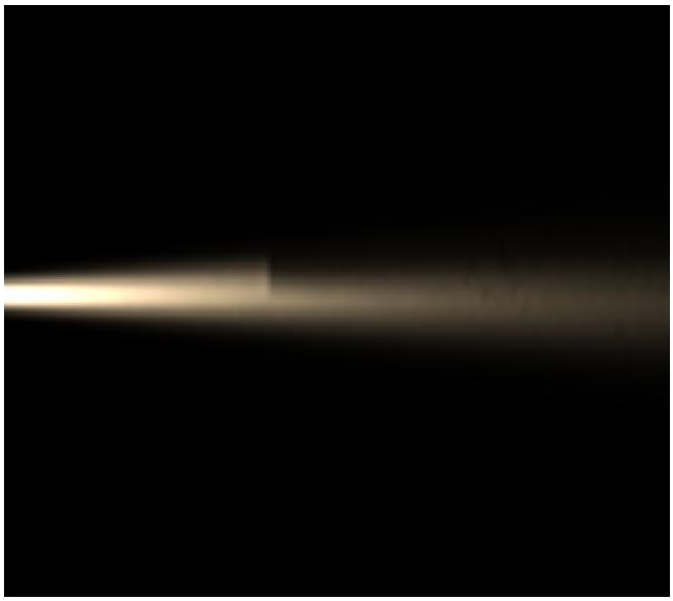

(d) $\theta = 135°$

Figure 5.13: Final scaled images for circular plasma injection

Chapter 6

Socioeconomic environment and impact

6.1 Project Budget estimation

In the present section, an estimation of the costs of the project is made. Costs can mainly be divided into direct and indirect costs. Direct costs are tightly related to the project while indirect costs are tangentially related to the project or the tasks included in the project.

Direct costs of this project include ECTS credits, labor costs, equipment and software. First, in the case of ECTS credits cost, it refers to the price paid by the student at the time of registration. Second, labor costs refer to the money that an Aerospace Engineer would have earned in the case of carrying out this project. Third, regarding the equipment, a laptop has been used to develop the tool in MATLAB, which is the software used for the tool generation.

- **ECTS credits**: At Universidad Carlos III de Madrid, an Aerospace Engineer student pays 26.51€per ECTS credit. This project is expected to be completed in 12 ECTS, which corresponds to 330 working hours. Therefore, the total price of this direct expense is detailed in table 6.1.

Description	Price / ECTS (€)	N. ECTS	Total price (€)
Student registration	26.51	12	318.12

Table 6.1: ECTS credits cost

- **Labor costs:** Regarding labor costs, an Aerospace Engineer intern earns on average 5€per hour in Spain (based on the companies that offer a paid internship position for UC3M students). As it has been mentioned before, 12 ECTS credits correspond to 330 hours of work.

Description	Average Salary (€)	Working Hours	Total cost (€)
Aerospace engineer intern	5	330	1650

Table 6.2: Labor cost

- **Equipment:** The only equipment used in this project is the laptop. Asumming a residual value of 200€after four years of expected working life and a straight-line depreciation model, the amortization of the laptop can be calculated and will be part of the expenses of the project.

Description	Price when purchased (€)	Residual price (€)	Working hours	Total cost (€)
Laptop	800	200	330	5.65

Table 6.3: Equipment

- **Software costs:** The software used to develop this tool is MATLAB, the price of a student MATLAB license is 35€. The present report is written in LaTeX, which is a free software for technical writing, thus, the cost of this software is 0€.

Taking into consideration the set of costs that this project involves and that have been just explained, it can be concluded that the total estimated direct costs of this project are 2008.77€as indicated in table 6.4.

Indirect costs of this project include the Internet service and power expenses. These costs can be estimated by calculating the price per hour of these services.

Expense	Price (€)
ECTS credits	318.12
Labor	1650
Equipment	5.65
Software	35
TOTAL	2008.77

Table 6.4: Total direct costs estimation

Assuming an average number of 30 days per month, the estimated indirect costs are detailed in table 6.5.

Description	Monthly payment (€)	Working hours	Total cost (€)
Internet	35	330	16.04
Power	40	330	18.33
TOTAL			34.37

Table 6.5: Total indirect costs estimation

Therefore, adding up together the estimated direct and indirect costs, it can be concluded the total budget of the project to be **2043.14€**.

6.2 Socioeconomic impact

This section is devoted to the analysis of the socioeconomic impact of the present project. Since it contributes to the development of plasma thrusters for space applications, the socioeconomic impact of this project can be understood as the impact of the use of plasma thrusters for spacecraft.

As explained in the introduction chapter, the use of plasma as a propellant for spacecraft engines results in a significant weight reduction during the whole space mission, from the spacecraft launch to the space trips. This weight reduction will decrease the amount of fossil fuels needed at the time of launch, making the space missions cheaper and more environmentally friendly. Moreover, for the same reason, the use of plasma engines while in space will allow the transport of heavier payload without an increase in the fuel needed for launch. Hence, it can be said

that if developed, plasma thrusters would have a positive environmental impact since they will contribute to save fuel.

Economically, the impact would also be positive, since space missions would become either cheaper due to the fuel savings or more cost-effective, being able to carry more payload for the same amount of fuel. Furthermore, the reduction of fuel volume at launch would result in a decrease of the volume of the fuel tanks with the corresponding material savings.

Nevertheless, the social impact of the use of plasma thrusters is hard to tell. Although space missions are aimed to explore and discover the unknown as well as to make human lifes easier and better in quality, these impacts, if any, would be long-term. If NASA's VASIMR plasma engine is able to reach Mars in 39 days, space journeys could become feasible at some point.

This being said, since this technology is not fully developed at the moment, there might be some negative effects derived from the use of plasma thrusters that are still unknown.

Chapter 7

Regulatory framework

The results of the present project do not depend on any kind of tests or experiments. Instead, they have been obtained through several computer simulations. There are no regulations about the calculation processes, therefore, no restrictions can be applied to this framework.

However, the space propulsion requirements are defined by the European Cooperation for Space Standardization (ECSS) in ECSS-E-ST-35C Rev.1 issued in March 2009. This standard defines the regulatory aspects that are common for liquid, solid and electric propulsion for both launch vehicles and spacecraft. The specific requirements for liquid and electric propulsion for spacecraft are defined in ECSS-E-ST-35-01C issued in November 2008. Although there exist some regulations about the electric propulsion in space, these will be properly updated when plasma electric engines are fully developed.

Finally, several patents can be found in the frame of plasma thrusters. Nevertheless, the most significant patent in this field is US 20150020502 A1 "Plasma thruster and method for generating a plasma propulsion thrust " by Serge Larigaldie, published in 2015. There are also other registration numbers for this patent in different world places such as Europe and China published in 2013 and 2014, respectively.

Chapter 8

Future Work

This chapter aims to state further actions to be taken to improve the computational tool that has been developed in this Bachelor Thesis. First, it would be really useful to test the tool and check its similarities with reality by performing some laboratory tests in order to check the accuracy of the tool.

The actual tool takes a long time to obtain high resolution images of the plasma flow. Therefore, a future task is to optimize the code in order to save computational time. Moreover, at the moment, the tool just considers Argon and Argon ions spectral lines. Nevertheless, another possible action that will spread the possible uses of this tool is to increase the elements in the database in order to use the tool for different plasma species such as Xenon or Krypton.

Furthermore, the code uses a partition function (Q) that has been approximated using NIST Atomic Spectral Database as a reference. Nevertheless, further investigation could be done in this field in order to develop an elaborated expression for the partition function, which is not constant but it slightly changes with the local temperature.

In the current project, the plasma jet is under Local Thermodynamic Equilibrium and therefore, the particle density for each energy level has been assumed to follow Boltzmann distribution. If non-equilibrium conditions are

considered, the particle density distribution would be different for each energy level and it should be specified, hence, opening a wide field of new results that have to be studied at some point.

Chapter 9

Conclusion

The objective of the present project was to develop a computational tool to perform two different tasks. First, starting from a prescribed flow field distribution, to obtain the spectra of Ar and Ar^+ at high spectral resolution. Second, to build the image of a plasma jet with the data obtained from computer simulations and the NIST Atomic Spectra Database.

For the purpose of the project, two different plasma jets simulations were addressed: in the first simulation, the plasma was injected through an ordinary circular section while in the second one, the ionized gas was injected through an annular section.

The data of the simulations was taken as input for the developed tool. These data were crucial for the obtention of the particle density distribution per unit volume using Boltzmann equation and the local emission. The local emission has been calculated over the whole jet volume, using different spectral resolutions, which can be set by the user of the tool.

The intensity was calculated using the `radon` function in MATLAB as a function of the angle of the plane of projection, which enables the image generation from different view references. This intensity has been filtered by the human eye sensitivity curves for every color (Red, Green and Blue) in a rudimentary manner

in order to produce images representative of the human eye vision.

In the tool, the user is free to set the desired filter instead of the human eye, in case any other type of radiation needs to be represented, for instance, IR or UV intensities which are in practice recorded with IR or UV systems, respectively. Also, the user can choose the spectral grid, resolution and z-sections of study.

The results obtained for the considered cases (ordinary circular and annular injection jets) have been analyzed. The final results have shown that the population density determines the colors displayed in the resulting images. Therefore, having a look at the outputs of the tool it is possible to identify the species present in a specific section of the jet. Also, the shape of the plasma injection affects the behavior of the particles and it is crucial for the derivation of the excitation temperature in the plasma jet.

Bibliography

[1] Griem, H. (2005). *Principles of plasma spectroscopy*. Cambridge (U.K.): Cambridge University Press.

[2] Stern, D. (2004).*Fisica del Plasma – Historia*. [Online]. Available at: https://www-istp.gsfc.nasa.go/Education/Mhplasma.html

[3] D. A. Gurnett, A. Bhattacharjee (2005). *Introduction to Plasma Physics: With Space and Laboratory Applications*. Cambridge, UK: Cambridge

[4] Ahedo Galilea, E. (2011). *Propulsión espacial por plasma*. Real Sociedad Española de Física, Vol 25(3)

[5] NASA Technology. (2016). *NASA - Ion Propulsion*. [Online]. Available at: https://www.nasa.gov/centers/glenn/about/fs21grc.html

[6] NASA's New VASIMR Plasma Engine Could Reach Mars in 39 days. (2016). Industry Tap Into News. [Online]. Available at: http://www.industrytap.com

[7] Wong, C. and Mongkolnavin, R. (2016). *Elements of Plasma Technology*. 1st ed. Singapore: Springer, pp. 49-98.

[8] Hutchinson, I. (2005). *Principles of plasma diagnostics*. 2nd ed. Cambridge: Cambridge Univeristy Press.

[9] Pérez Pemán, E. (2016). *Characterization of electric propulsion plasma jet by means of Optical Emission Spectroscopy*. Graduate. Universidad Carlos III de Madrid.

[10] Nave, R. (2005). *Quantum processes*. Georgia State University. [Online]. Available at: http://hyperphysics.phy-astr.gsu.edu/hbase/mod5.html

[11] Institutionen för Astronomi (2013). *Einstein Coefficients*. [Online]. Available at: http://www.astro.lu.se/Education/utb/ASTA21/pdf

[12] Conde, L. (2014). *An Introduction to Plasma Physics and its Space Applications*. Madrid: Universidad Politécnica de Madrid. [Online]. Available at: http://plasmalab.aero.upm.es/ lcl/PlasmaNotes/NotesPlasmaPhysics.pdf

[13] Aspects of Thermodynamic Equilibrium in Plasma. (2010). 62, pp.97-102. [Online]. Available at: http://bmif.unde.ro/docs/20101

[14] Cichocki, F., Domínguez, A., Merino, M., and Ahedo, E. (2016). *A 3D hybrid code to study electric thruster plume*. Space Propulsion Conference.

[15] Y. Babou, F. Cichocki, and A. Ahedo. (2016). *Hyperspectral tomography for Aerospace plasma flow investigations*. Equipo de Propulsión Espacial y Plasmas (EP2), Departamento de Bioingeniería e Ingeniería Aeroespacial, Universidad Carlos III de Madrid.

[16] 2014's launch tally highest in two decades. (2015). *Spaceflight now*. [Online] Available at: https://spaceflightnow.com/2015/01/04/2014s-launch-tally-highest-in-two-decades/.

[17] Méndez, D. (n.d.). *Our Engine*. [Online] Ad Astra Rocket. Available at: http://www.adastrarocket.com/aarc/VASIMR.

[18] Gottscho, R. and Miller, T. (1984). Optical techniques in plasma diagnostics. *Pure and Applied Chemistry*, 56(2).

[19] Benjamin-mills.com. (n.d.). *Electron configurations*. [Online] Available at: http://www.benjamin-mills.com/teaching/chemistry/GCSE/electron-configurations/

[20] Bogaerts, A., Gijbels, R. and Vlcek, J. (1998). Collisional-radiative model for an argon glow discharge. *Journal of Applied Physics*, 84(1), pp.121-136.

[21] Chemistry LibreTexts. (2016). *Periodic Trends: Ionization Energy*. [Online] Available at: https://chem.libretexts.org

[22] Nave, R. (2005). *Quantum processes*. [Online] Hyperphysics. Available at: http://hyperphysics.phy-astr.gsu.edu/hbase/mod5.html [Accessed 21 Jun. 2017].

[23] Kwok-san, L. and Shiu-sing, T. (n.d.). *Further physics - What is laser?*. [Online] Hk-phy.org. Available at: http://www.hk-phy.org/articles/laser/laser_e.html.

[24] Hwang, Shuen-Chen; Lein, Robert D.; Morgan, Daniel A. (2005). Noble Gases. *Kirk Othmer Encyclopedia of Chemical Technology*. Wiley. pp. 343-383.

[25] Lund University. (n.d.). *Einstein coefficients*. [Online] Available at: http://www.astro.lu.se/Education/utb/ASTA21/pdf/Einstein%20coefficients.pdf.

[26] NIST National Institute of Standards and Technology, U.S. Department of Commerce, NIST Atomic Spectra Database. [Online]. Available at: https://www.nist.gov/pml/atomic-spectradatabase.

[27] Northwestern University (n.d.). *What is the Doppler effect?*. [Online] Available at: http://www.qrg.northwestern.edu/projects/vss/docs/communications/3-what-is-the-doppler-effect.html.